Afshar-Mohajer Nima (Orcid ID: 0000-0002-6337-1824)
Dora Chandrala, Lakshmana (Orcid ID: 0000-0002-2695-9469)
Koehler Kirsten (Orcid ID: 0000-0002-0516-6945)
Katz Joseph (Orcid ID: 0000-0001-9067-2473)

Aerosolization of crude oil-dispersant slicks due to bubble bursting

Kaushik Sampath[1], Nima Afshar-Mohajer[2], C. Lakshmana Dora[1], Won-Seok Heo[1], Joshua Gilbert[1], David Austin[1], Kirsten Koehler[2] and Joseph Katz[1]

[1]Department of Mechanical Engineering, Johns Hopkins University, Baltimore, MD, USA

[2]Department of Environmental Health Sciences, Johns Hopkins Bloomberg School of Public Health, Baltimore, MD, USA

Corresponding author: Joseph Katz (katz@jhu.edu)

Key Points:

- Bursting of bubbles in slicks containing crude oil and dispersant mixtures aerosolizes the oil, generating micro- and nano-droplets.
- In ambient air, a ten-fold increase in sub-micron particle concentration occurs when large bubbles burst on slicks containing dispersants.
- Micro-droplets are generated for all bubble plumes and slick types, but their concentration decreases with increasing slick thickness.

This article has been accepted for publication and undergone full peer review but has not been through the copyediting, typesetting, pagination and proofreading process which may lead to differences between this version and the Version of Record. Please cite this article as doi: 10.1029/2018JD029338

Abstract

Bubble bursting is a primary source of marine aerosols, yet, little is known about particle emissions due to the bubble bursting in slicks containing oil-dispersant mixtures. In this study, bubbles with mode sizes of 86 μm (denoted as small), 178 μm (medium), and 595 μm (large) are injected into a seawater column covered by slicks of crude oil, pure dispersant, and dispersant premixed with oil at a ratio (DOR) of 1:25. The aerosol size distributions are monitored in the 0.5-20 μm and 10-380 nm ranges both in clean and ambient air environments. In ambient air, a ten-fold increase in sub-micron particle concentration occurs when large bubbles burst on slicks of 500 μm DOR-1:25 oil or 50 μm pure dispersant. Yet, in multiple tests performed at different ambient particle concentrations, the elevated size distributions persistently maintain the same shape as that of the ambient air. In contrast, smaller bubbles and tests not involving dispersants do not cause such an increase. Nano-droplets are also generated by large bubbles in particle-free air, but their concentrations are much lower. All plumes generate micron-sized aerosols, but trends vary. For the same contaminant, the micro-droplet concentration decreases with increasing slick thickness. Particularly striking is a reduction of two orders of magnitude in the micro-droplet concentration when medium and small bubbles burst on 500 μm crude oil slicks. Chemical analysis of air and particulates collected from filters sampling the particles confirm the presence of airborne oil above the slicks.

1 Introduction

Oil spills are associated with a broad range of immediate and long-term adverse environmental effects (Beyer et al., 2016; Gundlach & Hayes, 1978; Kingston, 2002; Teal, 1984). The implications on air quality include emission of micron- and nano-sized airborne fine particulate matter (Ryerson et al., 2011) and volatile organic compounds (VOCs) to the atmosphere (Middlebrook et al., 2011). Inhalation of fine particulate matter has been associated with a disruption in the cardiovascular system, respiratory function and pulmonary airway inflammations (de Haar et al., 2006; Neas, 2000; Rundell et al., 2007). Exposure to VOCs has been linked to headache, eye irritation as well as significant alterations in blood profiles and liver enzymes (D'Andrea & Reddy, 2013). Furthermore, the formation of organic aerosol downwind of spills has also been attributed to VOCs mixed with NO_x (Ryerson et al., 2011). The resulting atmospheric pollution concerns have led to the unprecedented application of dispersants to treat recent oil spills (Kujawinski et al., 2011).

These dispersants substantially reduce the oil-water interfacial tension, thereby accelerating the breakup of oil patches into small droplets and their dispersion in the ocean. Yet, there have been reports of increased exposure to oily aerosols resulting from the application of dispersants (Cini & Loglio, 1997; Zhou & Liu, 2001). Still, very few studies have characterized the aerosolization and transport of dispersant-treated oil spills.

Generation of oily aerosols involving semi-volatile compounds is a complex physiochemical process. It is well established that heavy n-alkanes present in crude oil tend to remain at the air-water interface (Liyana-Arachchi; et al., 2014; Vácha et al., 2006; Wick et al., 2010; Z. Zhang et al., 2016). This tendency is enhanced substantially by the addition of dispersants since their hydrophilic "head" preferably interacts with the water, and the hydrophobic tail attracts non-volatile n-alkanes to form near surface aggregates (Gill et al., 1983; Liyana-Arachchi; et al., 2014; Z. Zhang et al., 2016). Adsorption of these non-volatile aggregates by droplets generated by mechanical processes leads to their aerosolization.

Two processes associated with bubble-bursting from oceanic whitecaps, namely film (or cap) and jet breakups, are the primary sources for marine-aerosol emission (Cipriano & Blanchard, 1981; Veron, 2015). The cap forms when a rising bubble reaches an equilibrium position at the interface (Lhuissier & Villermaux, 2012). Film droplets with diameters ranging from 20 nm to 4 μm form as this cap drains, decreases in thickness and eventually shatters (O'Dowd & de Leeuw, 2007). The number of film droplets generated per bubble burst may exceed several hundred, increasing with the bubble diameter (Ke et al., 2017). Although most bubbles burst, film droplets are typically associated with bubbles larger than 1 mm in diameter. After bursting, capillary waves developing on the surface of the remaining cavity form a vertical liquid jet (Spiel, 1997b), which breaks up into droplets. Such breakup has been observed for bubbles with diameters ranging from 20 μm to 3.4 mm (Lee et al., 2011; Wu, 2002). With a size of about 5% of the bubble diameter, jet droplets are typically larger and fewer in number compared to film droplets (Spiel, 1994; Veron, 2015; Wang et al., 2017; Wu, 2002). However, a recent study has shown that jetting caused by 10-100 μm bubbles can also generate sub-micron droplets (Wang et al., 2017). Due to the difference in the generation mechanisms, jet droplets are composed primarily of the bulk liquid while film droplets are more representative of the surface (Veron, 2015). All the above studies involve aerosolization of clean seawater.

Sub-micron aerosols could be transported over intercontinental distances (Cachier et al., 1986). They are small enough to penetrate into the alveoli of the human respiratory

system (Heyder et al., 1986). Hence, generation of crude oil-dispersant sub-micron droplets might have adverse health implications (Major et al., 2012; Roberts et al., 2011). There is not much literature about the emission of crude oil-dispersant mixtures by bursting of bubbles. Recent experiments involving the simultaneous sub-surface injection of oil and bubbles into a seawater column (Ehrenhauser et al., 2014) provided data for the total airborne particulate matter measured above the surface. They confirmed that bursting of 550-870 μm bubbles caused emission of organic particles, and showed that premixing the oil with dispersant increased their total mass. Moreover, our preliminary tests near breaking waves impinging on oil and dispersant-contaminated seawater (Afshar-Mohajer et al., 2018), indicated that many of the particles aerosolized from the seawater when the oil slick is premixed with dispersant are small as 10 nm.

Combined with the potential health implications, these findings motivate systematic characterization of the concentration and size distribution of particle emission due to the bursting of bubbles on a water surface contaminated by oil slicks, with and without dispersant. Such measurements should involve a broad range of bubble sizes, and should detect nano- and micron-scale particles, the total mass of suspended particles (TSP), and the chemical composition of these particles. The present study is an attempt to address these challenges by injecting controlled bubble plumes into a vertical seawater tank with its surface exposed to ambient laboratory air and contaminated by slicks containing crude oil-dispersant mixtures. Comparisons between concentrations of airborne particles measured before, during, and after bubble-bursting events are drawn to study the emission of oil under various bubble plume and slick conditions. Additional experiments are also performed in a smaller tank with filtered air to re-examine sub-micron particle concentrations for certain bubble plume and slick conditions observed in the large tank.

2 Materials and Methods

2.1 Facility, oil properties, and bubble generation

Measurements have been performed in a large 2.0 m high and 0.6 m diameter cylindrical vertical tank illustrated in Figure 1a. The 1.6 m liquid column contains artificial seawater (Instant Ocean) with a salinity of 33 parts per thousand and a density $\rho = 1018.3$ kg/m^3. The bubble plume is generated by injecting pressurized seawater with the same properties through a custom-made nozzle illustrated in Figure 1b at a prescribed volumetric flow-rate (Q_w). Air is introduced at a controlled volumetric flow rate (Q_a) is introduced from

two radially opposite, 0.4 mm diameter ports located in the 0.4 mm throat of the nozzle. The water shears the injected air to generate a bubble plume. Similar approaches have been used in numerous prior studies (Hyunh et al., 1991; Parmar & Majumder, 2013; Sadatomi et al., 2012). The characteristic bubble size is adjusted by varying Q_a/Q_w. In the present study, Q_a is held constant at 20±0.4 cc/min, and Q_w is set to 13±2, 90±8 and 200±8 cc/min, resulting in three plumes containing what are referred to in this study as large, medium, and small bubbles, respectively for the same Q_a. Auxiliary tests with the same bubble generator nozzle have also been performed in a smaller sealed tank (Figure 1c), with a headspace of 31.5 L.

The injection of bubbles into the tank results in a slight increase in the water level. This increase is less than 1.5 cm after injecting small bubbles (largest Q_w) for 20 min, and corresponds to a change of 0.9% in the bubble rise distance. Moreover, having an outflow to compensate for this small change may introduce secondary flows that might affect the bubble plume characteristics, as well as, result in transport of oil or dispersants out of the tank. Hence, there is no outflow of water during the present experiments and the effects of the fractional change in bubble rise distance are assumed to be negligible.

Louisiana Light Sweet crude oil (MC-252 surrogate) is 'freshly drawn' from the barrel before each test. In some of the tests, as indicated, the oil is premixed with Corexit 9500A (Nalco Environmental Solutions LLC) dispersant at a dispersant to oil ratio (DOR) of 1:25, referred to as 1:25 DOR. Additional tests are performed using the same dispersant without oil. The seawater-crude oil interfacial tension is measured using the pendant drop method (Rotenberg et al., 1983; Song & Springer, 1996). However, this approach is not suitable for DOR 1:25 oil and pure dispersant. Hence, their interfacial tension is calculated from the oblateness of sub-millimeter (0.35-0.55 mm) droplets rising in quiescent seawater (Bozzano & Dente, 2000; Hu et al., 2000). The measured values for crude oil, 1:25 DOR and dispersant are 18.58±0.09, 0.13±0.004, and 0.09±0.008 mN/m, respectively, in agreement those reported in prior studies (Murphy et al., 2015). The density (ρ), dynamic viscosity (μ), surface tension (σ) adapted from various sources (Murphy et al., 2015; Nalco Company, 2008; Steffy et al., 2011) and the above measured interfacial tension values with seawater (γ) for crude oil, DOR 1:25 and pure dispersant with seawater are provided in Table 1.

Following (M. M. Zhang et al., 2010), planar fluorescence imaging is used to measure the sub-surface bubble size distributions. A sample area of 20.6×13.8 mm located at the center of the tank is illuminated with a 3 mm thick vertical laser sheet originating from a 120 mJ/pulse Nd:YAG laser (Figure 1). Trace amounts of Rhodamine WT (Sigma Aldrich) dye

are mixed with the seawater column, converting the entire sample area into a fluorescent light source, which illuminates the bubbles passing through it. Images of the sample plane are acquired using a 4872 × 3248 pixels CCD camera after filtering the laser wavelength (532 nm) out using a high-pass optical filter (560 nm). Reflection of the surrounding fluorescence from the bubble surface, combined with the absence of emission from the gas, generates rings defining the boundaries of bubbles. This occurs as long as the bubbles are sufficiently smaller than the sheet thickness. A sample image is shown in Figure 2a. Statistically independent samples that do not contain the same bubbles are obtained by recording a series of images at 3 frames per second.

Data analysis starts with image enhancement, which includes subtraction of the time-averaged background, followed by Modified Histogram Equalization (MHE) (Roth & Katz, 2001) to extend the intensity distribution to the full dynamic range of the 8-bit images. Two-dimensional segmentation then provides a list of candidate bubbles. Since some of the detected bubbles are slightly out of focus, we use the intensity gradients shown in Figure 2b to select and retain the in-focus images for subsequent analysis. The selection is based on a comparison of the top 10% of the gradients along the perimeter of each bubble to a global threshold. For the example provided, Figure 2c shows the enhanced image of bubbles retained after the gradient-based selection process. In some cases, the enhanced traces are contaminated by background noise. Under the assumption that all bubbles in this size range are nearly spherical, the noisy traces are identified and removed by setting a threshold on the eccentricity of the images. Subsequently, the centers and radii of the bubbles are calculated using the Circular Hough Transform built into the MATLAB function: imfindcircles (Atherton & Kerbyson, 1999; Yuen et al., 1990). Probability histograms of the detected bubble size distributions for the plumes containing large, medium and small bubbles are shown in Figure 2d. They are based on all three replications performed for each bubble case, and the mean is shown in Figure 2c. The corresponding mode diameters (d_b^*) are 595, 178 and 86 μm, and the mean diameters ($\bar{d}_b$) are 614, 263 and 89 μm. The size distributions of the plumes containing the small and medium bubbles have single modes, while those of the large plume are multi-modal, with one of them dominant. The medium bubble plume has the broadest distribution that partially overlaps with the other two.

To test the repeatability in size distributions, three independent tests, each involving acquisition of 2000 images, have been performed for the three plumes. Trends, demonstrated in Figure 2e, show that for the large, medium and small bubble plumes, the modes differ by

maximums of 5.4%, 6.9%, and 2.4% respectively, and the corresponding standard deviations differ by maximums of 5.6%, 3.8%, and 2.3%, respectively. Hence, the test conditions for different runs appear to be repeatable. Using the size distributions to calculate the volume distribution and Q_a, one can estimate the flux of bubbles generated by each plume. The resulting values are 2.66×10^3, 2.32×10^4, and 6.65×10^5 per second for the large, medium and small bubble plumes, respectively.

In addition to the detection of bubbles in the laser sheet, observations have also been performed to determine the likelihood of bubble coalescence near the surface for seawater, and for the 500 μm thick crude oil slicks. These observations show that for the present test conditions, such events are extremely rare, and do not have a significant effect on size and flux of bubbles.

2.2 Measurements of particle emissions

The distributions of micron- and nano-sized particles, as well as TSP, are sampled 10 cm above the free-surface (Figure 1a). The distribution of nano-sized particles (10-370 nm) (also referred to as nano-droplets) is sampled every minute using a Scanning Mobility Particle Sizer, SMPS model 3938 (TSI Inc.), with an electrostatic classifier model 3082 and a condensation particle counter model 3787. An impactor with an orifice diameter of 0.071 cm installed at the inlet of this classifier removes particles larger than 0.5 μm. The SMPS is equipped with an advanced aerosol neutralizer (Model 3088, TSI Inc.) placed after the inlet and before the introduction of the aerosol into the differential mobility analyzer. As discussed in (Hinds, 1999), more than 97% of the particles smaller than 100 nm do not carry charges after passing through this X-ray based device. Hence, it is not expected that the residual charges on the aerosol are a significant contributor to the present data. The SMPS parameters for the small and large tank tests are identical.

The size distribution of micron-scale particles (0.5-20 μm) (also referred to as micro-droplets) is sampled every 20 seconds using an Aerodynamic Particle Sizer, APS model 3321 (TSI Inc.). Although the sampling and sheath flow rates of the SMPS may be adjusted to avoid a gap in the size range between 380-500 nm, the present range has been chosen because of the following considerations. First, broadening the size range requires lowering the ratio of the sheath flow rate to the sample flow rate. The resulting reduction in the kinematic resolving power of the differential mobility analyzer has been known to reduce the reliability of the SMPS data (Flagan, 1999; Kulkarni et al., 2011). Second, although, a continuous range

may be achieved by shifting the SMPS range to higher values, it will limit the smallest sampled particle size to 14 nm or larger. As mentioned earlier, in view of the high concentration of 10 nm droplets measured above breaking waves (Afshar-Mohajer et al., 2018) the present study aims at studying the effects of bubble-bursting in oil-dispersant contaminated slicks on particles as small as possible.

The TSP mass is collected using a closed-face 37-mm filter cassette connected to a vacuum pump, as suggested by the NIOSH Method 0500 (Eller, 1994). The filter material is fluorocarbon-coated glass fiber (FiberFilm T60A20, by Pall Inc.) and the suction flow rate is 4 L/min. The filter weights before and after sampling are measured using an analytical micro-balance, model MX5 (Mettler Toledo Inc.), at a precision of 1 μg. Before weighing, the filters are equilibrated in a room under controlled temperature (21 ± 3 °C) and relative humidity (30 ± 2 %) for at least four hours.

Each large-tank experiment consists of a pair of runs, a baseline case with clean seawater alone, followed by a run with a contaminant slick. For each run, data is acquired for a total of 40 min, including 10 min before, 20 min during, and 10 min after bubble injection. Test are performed for slicks of crude oil and DOR 1:25 with thicknesses of 50 and 500 μm, as well as a 50 μm slick of pure Corexit 9500A. The volume required to form a slick of the prescribed thickness over the entire tank area is poured gently and distributed as uniformly as possible over the surface. Images of the slicks have been acquired (not shown) to verify their uniformity. For the slicks with dispersant and all the 500 μm slicks, a continuous layer covers the entire surface. However, for the 50 μm crude oil slick, a series of smaller patches distribute uniformly over the entire surface. Each case is tested for the large, medium and small bubble plumes, resulting in a total of fifteen different experiments as shown in Table 2. Several experiments are repeated three times to confirm and quantify repeatability in trends.

The large-tank cleaning protocol after each experiment consists of the following series of procedures. First, the air volume in the space between the free-surface and the plate supporting the instruments (Figure 1a) is pumped out at 250 L/min for five minutes into a fume-hood and replenished with fresh room air. The air conditioning system in the laboratory is equipped with a MERV 14 filter, that according to ASHRAE 52.2-1999 standards has a filtering efficiency of 75-85% and 90% for 0.3-1 μm and 1-10 μm particles respectively. Then, the plate is removed, and the contaminated surface is skimmed with oil adsorptive pads (New Pig Ltd.). The tank is drained and its walls are washed/scrubbed thoroughly with a soap solution, as well as rinsed with tap water and wiped dry with low-lint optical wipes

(Kimberly-Clark Corporation). The rinsing and wiping steps are repeated another time before filling the tank with the same volume of seawater for the next run. Before starting the next run, the air above the surface is vacuumed again at 250 L/min for five minutes and replenished with filtered air.

The air volume between the free-surface and the support plate is not sealed for the large tank. Hence, the sampling instruments entrain ambient air from the periphery of the plate to meet their sampling requirements (i.e. 1, 1.5 and 4 L/min for the APS, SMPS, and TSP respectively). Therefore, air containing the aerosolized content is mixed with ambient air. The baseline tests performed before each experiment, with or without oil/dispersant slicks, provide reference concentrations that are subsequently compared with those measured during and after bubble injection. The APS is mounted on the supporting plate such that only its sampling port is exposed to the volume above the free-surface. Such proximity becomes necessary in order to sample as many micron-sized particles. The rest of the instrument (including its exhaust) is located above the plate and discharges into the ambient air above the plate. The APS is equipped with two 9922-11-BX filters positioned in series at its exhaust pump, each rated to filter out 99.99% of 100 nm particles (Balston OEM, 2015). Hence, it is assumed that the small fraction of the APS exhaust that may be 're-sampled' has a negligible impact on the present findings. The TSP and SMPS are located well outside the tank, with only their sampling tubes introduced into the chamber. Their exhausts are diffused effectively into the room and are not expected to affect the present measurements.

To elucidate some of the phenomena observed in the large tank, a series of experiments have been performed in a smaller-scale sealed tank (Figure 1c) focusing on trends in sub-micron particle concentrations. The experiments have been performed using: (i) HEPA-filtered clean air, with nano-aerosol background concentrations of ~20 #/cc, consistent with other bubble chamber studies (Sellegri et al., 2006), and (ii) unfiltered ambient air. In the filtered air case, the air is circulated through the HEPA filter prior to the run, and then after introducing the contaminant layer to replenish the air pumped by the SMPS. These tests are performed using the same bubble generator, maintaining the same Q_a and Q_w as before. The size distribution of large bubbles in the small tank, which is also presented in Figure 2, has a single peak at 620 μm, only slightly higher than that of measured in the large tank. Sub-micron particle concentrations are recorded for the baseline case, as well as slicks of 500 μm crude oil, DOR 1:25, and 50 μm pure dispersant. Data are acquired for 10 min before (0-10 min), 20 min during (10-30 min), and 30-60 min (30-60/90 min) after bubble injection, the

latter being significantly longer than the large tank experiments. Table 2 also lists the experiments performed in the small tank.

The temperature and relative humidity (RH) of the sampled air from the SMPS during all the experiments vary between 23.8–25.6 °C and 55-65%, respectively. The RH at the inlets to the SMPS and APS is initially approximately 20% and increases to a steady state condition of around 55% once bubble bursting begins. The hysteresis effect for the salt droplets results in a particle size distribution that is a strong function of RH. The present number size distributions show the measured values, not the dry particle diameters. The latter can be estimated using particle growth factors reported recently (Zieger et al., 2017). Based on their findings, the hygroscopic growth factor of sub-micron sea salt droplets at 55% RH ranges between 1.4-1.5. Therefore, the dry particle diameters can be approximated by dividing the present values by 1.4-1.5. For droplets/particles that contain both salt and oil or for ambient particles, however, the relevant growth factor is expected to be lower.

3 Results

3.1. Sub-micron particle concentrations – large tank experiments

The background distribution of airborne nano-sized particles in the room varies between runs due to several external factors (Matson, 2005; Salimi et al., 2013; Q. Zhang & Zhu, 2012). For the present data, it varies around 10^2 – 10^3 particles/cc across the entire size range. However, for the same run, the background distributions before, during, and after bubble injection are essentially the same (without the presence of oil and/or dispersant). To quantify this, the time evolution of the total nano-aerosol concentration for all the baseline tests, where bubble-bursting induced changes in concentration are insignificant, is shown in Figure S2. The standard deviations of the respective baseline tests are listed in Table S2, expressed as a fraction of their time-averaged value. As evident, the changes are in the range 2-13%, precluding meaningful discussions about trends in the nano-size concentration that fall in this range for large tank tests in ambient air.

The corresponding size distributions of nano-sized particles for all conditions are shown in Figure 3. Colors denote the different contaminants and slick thicknesses. For each color, dashed and solid lines represent runs without (baseline) and with contaminant slicks, respectively. The data are time-averaged over 10 min before (left column), 20 min during

(middle column) and 10 min after (right column) bubble injection. The results for the large, medium and small bubble plume cases are presented in the top, middle and bottom rows, respectively. To demonstrate the impact of background variability on the results, and show that it still allows us to determine the effect of bubble size and oil properties on the generation of aerosols, Figure 3 contains data for one of the three runs. Having data recorded prior to the injection of bubbles for each case enables us to subtract the background contribution from the aerosol generated during and after bubble bursting. Furthermore, some tests have been replicated three times, as listed in Table 2, to verify that they show similar trends regardless of the background size distribution. Figure 4 shows the average size distribution for selected cases and the baseline after subtracting the background concentrations prior to bubble injection. The error bars show the distribution of standard error, i.e. the standard deviation between runs divided by $n^{1/2}$, when n is the number of replicates.

The following prominent trends in the sub-micron particle concentrations are observed in the large tank experiments (Figures 3 and 4): (i) During bubble injection, two conditions cause an order-of-magnitude increase in the nano-sized particle number concentration, i.e. injection of large bubbles into a 500 μm thick slick containing 1:25 DOR, and into a 50 μm layer of pure dispersant. To assure that these increases are repeatable, both tests have been replicated n=3 times, and as Figure 4 clearly shows, all have similar trends. The medium and small bubbles do not seem to affect the size distributions in all cases. (ii) In spite of the increases in magnitude, in both cases, the size distributions still have similar shapes as those of the ambient particles prior to bubble bursting, raising concerns about the impact of the ambient particles on the measurements. (iii) These elevated concentrations persist even 10 min after bubble injection has stopped. (iv) For all the other test conditions, the changes to the nano-sized particle number concentrations before, during, and after bubble injection are of the same magnitude as the variability in background concentrations. In most of these cases, the shape of the size distribution remains similar.

3.2. Sub-micron particle concentrations – small tank experiments

A series of tests have been performed in a small tank to elucidate the trends in the sub-micron particle concentrations observed in the large tank, in particular the effect of ambient air. The first series of measurements examine the airborne nano-sized particle number concentrations above the various slicks with HEPA-filtered air above them. Results for plumes containing

large and small bubbles are presented in the top and bottom rows of Figure 5, respectively. The data are time-averaged over 10 min before (left column), 20 min during (middle column), and 60 min after (right column) bubble injection. The color scheme used for the different slicks in Figures 3 and 4 is also used in Figure 5. For cases with three replicates (see Table 2), the plot shows the average values, and the error bars denoting the standard error. In cases with only two replicates, both results are plotted using the same color, but with different line shapes. As expected, the concentration of nano-particles prior to bubble injection is extremely low. Bursting of large bubbles on slicks of 500 μm DOR 1:25 oil and 50 μm pure dispersant increase the number concentration of airborne nano-particles from ~2/cc to a maximum of ~60-80/cc. In both cases, the distributions have a single broad peak at ~130 nm. For crude oil without dispersant, the nano-droplet concentration is negligible, and for the baseline case (no slick), the peak is only ~15/cc, also centered around 130 nm. Hence, the slicks containing dispersant increase the concentration of nano-particles relative to the baseline or prior to bubble injection, but the increase is much smaller than those observed in the presence of ambient air. The small bubble plumes cause only a marginal increase in concentration to ~20/cc for the two slicks containing dispersants, and to ~8/cc for the baseline case. This trend is also consistent with the negligible impact of small bubble plumes in the large tank.

Next, we compare results obtained for clean and ambient air in the small tank, focusing on large bubbles and a 500 μm thick slick of DOR 1:25 oil. Figure 6 shows the time-averaged number concentrations for 10 min before bubble injection (Figure 6-a, f), for 20 min during (Figure 6-b, g) injection, as well as 0-10 min (Figure 6-c, h), 10-20 min (Figure 6-d, i) and 20-60 min (Figure 6-e, j) after stopping the bubble injection. The first row shows results for clean air (Figure 6a-e), and the second row, for tests performed with ambient air (Figure 6f-j). For the clean air, the increase in concentration during injection, the size corresponding to peak concentration, and the immediate decay after the bubble injection stops are consistent with the trends shown in Figure 5. As for the tests performed with ambient air, three trends are evident: (i) Bubble injection increases the number density of airborne nano-particles, but the increase is more moderate (from ~ 3500/cc to ~8000/cc) than that observed in the large tank. This latter trend may be attributed to, e.g., the smaller diameter of the plume when it reaches the surface resulting from the ~5.7:1 ratio in the distance between the injector and the surface. (ii) The initial shape of the distributions for the two replicates is different (they were performed on different days), but consistent with the

observations in the large tank, this shape (but not the magnitude) is maintained throughout the experiment, i.e., it is not altered by the bubble injection. Plausible mechanisms that might affect this phenomenon are introduced in the discussion section. (iii) The decay in concentration after injection stops is slower than that observed for clean air.

The next experiments are aimed at understanding the slow decay in nano-particle concentrations in the presence of ambient air after bubble injection stops. Figure 7 compares the time evolution of total particle concentration in the large tank (LT) with those observed in the small tank (ST) for both ambient and clean air. Specifically, it shows the evolution of

$$\chi = \frac{C(t) - \overline{C_{t<10\ min}}}{C_{t=30min} - \overline{C_{t<10\ min}}}$$

where C is the concentration over the entire measured size range, $C_{t=30min}$ is the concentration when bubble injection stops, and $\overline{C_{t<10\ min}}$ is the time-averaged concentration before bubble injection starts. For the large tank data, the results are averaged over three replicates (Table 2), and for the small tank tests, the results for two replicates are shown separately. Additional tests have been performed following the suggestions of one of the reviewers of this paper that the slow decay might be associated with particle storage on the tank-wall during bubble bursting, and subsequent release of this aerosol after injection stops. In these tests, the entire interior walls of the headspace in the small tank are covered with oil adsorptive pads (New Pig Ltd.). The results are also included in Figure 7, focusing on changes occurring after bubble injection stops. Trends observed before and during bubble injection are not significantly different than those obtained for the unpadded walls, hence they are not shown.

In experiments performed with clean air, the decay in nano-aerosol concentration is already noticeable 3 min after injection stops, while for all the data acquired with ambient air, the decay rate remains small for the first 27 min. This initial minimal decay in both tanks suggests that this trend persists regardless of setup and initial concentration. With the 1.5 L/min sampling rate of the SMPS and a headspace of 31.5 L in the small tank, without additional production, the concentration of particles at t=51 min should decrease to 1/e of the level at t=30 min (when bubble injection stops). Yet, Figure 7 indicates that in the presence of ambient air and unpadded walls, the nano-aerosol concentration hardly changes. In contrast, while the particle concentration with padded walls persists for the first 10-12 min, it subsequently decays rapidly, at a rate that is similar to the results obtained for clean air. This

trend plausibly suggests that in the absence of padding, the nano-particles are stored on the walls of the tank during bubble injection, and then become airborne after it stops. Such re-aerosolization might be associated with e.g. drying of the tank walls.

3.3 Micron particle size distributions

The micron-sized particle concentrations are shown in Figure 8, plotted in the same manner as Figure 3. For all cases, the aerosol size distributions prior to bubble injection are low and most collapse onto a power slope of around -0.6, with concentrations that do not differ significantly from each other. This consistency confirms that the starting conditions for all the experiments are very similar and that the procedures used for spreading the contaminant layers have not generated aerosolized particles, at least in the micron scales. Second, injection of bubbles causes a substantial increase in the concentration of micro-aerosols, but trends vary with bubble size and layer properties.

For the baselines, in these plots, which match the total gas volume for all cases, the bubble-induced change in concentration increases with bubble flux. This trend will be revisited during subsequent analysis, which is based on the number of droplets generated per bubble. The large bubbles increase the slope of the number size distributions (from -0.6 to -0.15), but it remains negative. Conversely, the size distributions corresponding to the medium and small bubble plumes peak in the 2-5 μm range, with concentrations of 50-90/cm^3 and 300-400/cm^3, respectively.

For the two crude oil layers, large bubbles increase the concentration of micro-droplets relative to the corresponding baselines, and the effect of the layer thickness is minimal. In fact, the crude oil cases are the only ones where the aerosol concentrations are higher than the baselines. Conversely, both crude oil layers reduce the concentration of droplets for the small and medium bubbles, particularly for the 500 μm layer, where the number density decreases by several orders of magnitude compared to the baselines. As discussed later, this reduced aerosol production is caused by entrapment of the small and medium bubbles under the oil layers, where they form clusters, and sometimes coalesce before penetrating the oil layer.

For both DOR 1:25 oil layers exposed to large bubbles, the results are very similar to the baselines for droplets smaller than ~5 μm, but are lower at larger diameters. For medium and small bubbles, the contaminated layers reduce the generation of micro-aerosols across all sizes, with the concentrations decreasing with increasing thickness. However, the decrease is

not uniform, with a reduction of nearly two orders of magnitude for droplets smaller than 2 μm, and only a slight change for larger ones. Hence, the preferred modes for these contaminated cases fall in the 2-5 μm range. As for pure dispersant, injection of the large bubbles hardly increases the concentration of micro-droplets, resulting in the largest reduction compared to the baselines. The medium and small bubble results also show a substantial decrease compared to the baselines across all sizes, but especially for droplets smaller than 2.5 μm, resulting again in a peak between 2-5 μm. Furthermore, it appears that the transition at ~2.5 μm becomes sharper with an increase in volume of dispersant near the interface.

The repeatability tests for the micron range are summarized in Figure 9. Here again, the results of three replicates are averaged and the backgrounds prior to injection are subtracted, with the error bars indicating the standard error. The missing data points correspond to cases where the average concentration is lower than the background. As evident, the replicated tests show essentially the same trends.

After the bubble injection stops, in most cases, the micron-sized number concentrations decrease rapidly to approximately the starting value. The only two exceptions correspond to pure dispersant for small and medium bubble plumes, where distinct modes centered around 3-4 μm persist. The peak generated by the small bubbles is about an order of magnitude higher than that generated by the medium bubbles. Based on visual observations, it appears that the dispersant stabilizes the bubbles in the liquid column, lowering their rise velocity, and causing a significant delay in bursting. Indeed, the concentrations revert to their initial values after a longer time period, beyond the present range of systematic measurements. A reduction in the rise-velocity with increasing concentration of surfactants such as sodium dodecyl sulfate (SDS) that are present in oil dispersants has been reported in prior studies (Fdhila & Duineveld, 1996).

For all the conditions measured by the SMPS (Figure 3), there is a sharp reduction in the number concentration of particles larger than 200 nm. This trend continues into the APS measurement range (Figure 8) for many conditions. Due to the differences in trends, the nano-scale and micro-scale results are presented in different plots and discussed separately. Figure S3 shows the combined particle number distributions measured from the APS and SMPS for all the large tank data presented in Figures 3 and 8 without any size corrections. However, in spite of the size gap between the two sets, for all cases, the distributions are

continuous, with the SMPS data ending around 10#/cc for 380 nm particles, in the same range as the 0.5 μm particles in the APS data, as shown in Figure S3.

3.4 Micron-particle emission factors per bubble

To make the present data relevant for modeling and predictions of aerosol generation in polluted marine environments, it is useful to calculate the distributions of number and mass of aerosols generated per bubble. They are referred to as the number-based (EF_n) and mass-based (EF_m) emission factors. In all cases, the measured particle number concentrations before injection are used as a background and subtracted from those detected during injection. Hence, the data represents the time-averaged net addition of particles occurring during bubble bursting. For particles in the micron range, the volumetric flow rate of the APS is used for converting the time-averaged net concentrations to net droplet-fluxes. The results are then averaged over all the replicated experiments for the same condition (Table 2). All the baseline datasets for a specific bubble plume are also averaged into a single curve.

Based on the differences between the sub-micron particle number concentrations for the same bubble plume (Figures 3, 5 and 6), it does not yet appear clear whether bubble-bursting is the only factor that determines the generated particle count. Other factors such as ambient air quality, plume width, surface area, etc. may also contribute to the observed value. Therefore, we confine the calculations of EF_n and EF_m to the micron particle concentrations. The bubble fluxes are calculated based on the rate of gas injection into the nozzle and the mean bubble volumes, assuming that all of the bubbles burst, and ignoring potential secondary effects, such as coalescence. Then, EF_n is the ratio of particle to bubble fluxes. Similar procedures have been used in prior studies involving pure seawater (Wang et al., 2017). Since the particle compositions are unknown, the density of pure water along with the known particle volume is used to calculate EF_m in pg/bubble. The distributions of EF_n and EF_m for micron-sized droplets are shown in Figure 10. The mode of each distribution and the total number of detected droplets per bubble, i.e. the sum of EF_n over all the sizes ($\sum EF_n$) are also summarized in Table 2.

As expected, for a specific bubble plume, the effect of oil properties on EF_n and EF_m do not differ from those presented in Figure 8, but the variations among plumes are substantial. For the large bubble plume, the modes of EF_n of micro-droplets fall in the 0.8-1.5 μm range, and the corresponding modes of EF_m are 7-11 μm (Figure 10 a, d). The magnitude of the latter modes for slicks with dispersant in the micron range is significantly smaller than

those associated with crude oil or baseline. The modes of EF_n associated with medium and small bubble plumes fall in the 1.7-6.2 μm range, i.e. they are larger than those generated by the large bubbles (Figure 10 b, c and Table 2). This size difference decreases when results are expressed in terms of EF_m, where the modes for the three plumes fall in the 6-10 μm range (Figure 10 d, e and f). Except for the 500 μm crude oil slick, the peak values of EF_n and EF_m for the medium bubbles are higher than those of both the large and small bubbles.

3.5 Total suspended particulate (TSP) mass and chemical analysis

Assuming that all the suspended particulate mass collected on the TSP filters during each experiment is only caused by bubble-bursting, the TSP mass per bubble (TSP_B) is calculated by dividing the TSP mass accumulated over the entire 40 min test by the number of injected bubbles (over 20 min). The data shown in Figure 11a are averaged over the available (n) replicates for the same condition, with error bars denoting the standard error. To facilitate a comparison of TSP_B to the micron particle size distributions, that presumably dominate the aerosol mass collected, we calculate the sum of EF_m over all the measured micron sizes and denote it as $\sum EF_m$. However, since the pumping rate of the APS (1 L/min) is different than those for the TSP (4 L/min), the values of $\sum EF_m$ are multiplied by the corresponding volumetric flow rate ratio (4/1 for the APS) to obtain $\sum EF_m^{corr}$ presented in Figure 11b. Further, Figure 11c-d is shown to focus on the effect of the oil layer thickness on the total suspended particle mass.

As evident, for most cases, there is a good agreement in the trends of TSP_B and $\sum EF_m^{corr}$ with varying oil properties and bubble sizes. Such an agreement between independent sensors adds credibility to the present findings. The two values also lie within the same order of magnitude, but those corresponding to $\sum EF_m^{corr}$ are persistently higher. A possible reason for this may be evaporation during the equilibration step before the filters are weighed. Moreover, the extended drying of the filters in the 10 min after bubble injection could also contribute to this difference. Most notable observations are: (i) the very low TSP_B values for the 500 μm crude oil slick exposed to small and medium bubbles; and (ii) the higher TSP_B of the medium size bubbles compared to large and small bubbles except for the pure dispersant and the 500 μm crude oil layer.

Additionally, in order to evaluate whether the airborne particles contain oil and/or dispersant, preliminary chemical analyses have been performed, as summarized in the supporting information. The first method involves Gas Chromatography/Mass Spectrometry

(GC/MS) of gas and particulate emissions collected above slicks of 500 µm crude oil, DOR 1:25 oil as well as 50 µm pure dispersant with large bubble plumes. Results described in Table S1 report the presence of similar concentrations of hexane, cyclohexane, and heptane in both the crude oil and DOR 1:25 oil cases, confirming that the droplets and/or volatile compounds above the DOR 1:25 oil slicks contain crude oil. Conversely, the samples collected above the pure dispersant slicks contain negligible amounts of these compounds. Second, Fourier Transform Infrared Spectroscopy (FTIR) of the TSP filters collected from different tests have been compared to reference spectra obtained for drops of pure crude oil and dispersant placed on unused TSP filters. Absorption spectra that are shown in Figure S1 confirm the signatures of crude oil in the samples collected above crude oil and DOR 1:25 oil slicks with large and small bubble plumes. Further details of the methodology, associated results and findings are provided in the Supporting Information.

4 Discussion and Conclusions

4.1 Micron particle emissions

The discussion starts with a comparison between the present number and size of micron-sized aerosolized droplets to trends reported in the substantial literature for jet drops generated in clean seawater (Lee et al., 2011; Spiel, 1994, 1997a, 1998; Veron, 2015; Wang et al., 2017). The commonly used scaling for the top jet droplet diameter as a fraction of the originating bubble diameter is 5%, or the so-called "5% rule" for wet droplets (80% RH). For the dry particle diameter, this translates to 2.5% (C.F.Kientzler et al., 1954; Wang et al., 2017).

Accordingly, the expected jet droplet sizes for the large bubbles should be between 16 and 31 µm, a fraction of which would fall outside the measurement range of the APS. However, as Figure 8, Figure 9 and Figure 10 show, there is no evidence of such a peak for any of the large bubble plumes. A likely explanation for this disagreement involves the effect of gravity on the droplet trajectories. The present sampling ports are located 10 cm above the free surface (Figure 1), and the previously measured maximum ejection height of droplets ejected from 600 µm bubbles is less than 5 cm (Blanchard, 1989; Lewis; & Schwartz;, 2004), with settling velocities greater than 0.3 cm/s (Guazzelli et al., 1988). Hence, the present results, including those of the TSP_B, account for smaller droplets. Accordingly, further discussions about the micron-scale droplets are restricted to the small and medium bubble plumes.

The small and medium bubble plumes do not cause a substantial increase in the nano-droplet concentration, and their bubble size falls well below that typically associated with film droplets (Blanchard & Syzdek, 1988; Resch et al., 1986; Veron, 2015). Hence, the subsequent comparisons assume that the small and medium bubble plumes generate jet droplets. The present baseline droplet fluxes, after accounting for growth corrections (as detailed in Section 2.2), in the micron range are compared to those predicted by the 5% rule for the small and medium bubble plumes. The droplet fluxes are estimated by multiplying the measured concentration of micron-size particles averaged over several runs (Figure 9b and c) by the sampling rate of the APS (1 L/min), and by the ratio of the total pumping rate of all the instruments to that of the APS. The results of this comparison are expressed as the number of droplets per second and shown in Figure 12. As is evident, for both plumes, the predicted fluxes are narrower than the measured ones. This trend is consistent with studies (Spiel, 1994; Wu, 2002) showing that the 5% rule only applies to the top jet drop and that the size of other jet drops varies. For the small bubbles, the measured flux and size are in good agreement with the predicted values in the 1.7 – 6 μm range, with $\sum EF_n$=1.27 (Table 2). Hence, the assumption of a single jet drop per bubble, i.e. $\sum EF_n \sim 1$ seems reasonable for this size range, in agreement with recent studies (Lee et al., 2011; Wang et al., 2017). However, the results for the medium bubble plume ($\sum EF_n$=8.02) do not agree, indicating that more than one droplet is generated by each bubble. For this size range, the number of jet drops reported in the literature (Lewis; & Schwartz;, 2004; Veron, 2015; Wu, 2002) is about 6-8 per bubble, most of them smaller than that predicted by the 5% rule. Hence, one should expect a downward shift in the size and a larger droplet flux. Figure 12 shows that the flux of 3-5 μm droplets is about five times higher than the predicted peak at 6-10 μm. For convenience, comparisons between the droplet modes, scaling and fluxes with literature are provided in Table 3. It appears that the present trends are consistent with the published results.

A noteworthy factor that is not accounted for in the present analysis is the coalescence of bubbles below the surface, which, may increase the values of $\sum EF_n$. Overestimation of the bubble counts may occur if the bubble flux and surface lifetime are sufficiently high. The presence of crude oil, DOR 1:25 oil or dispersants on the surface may increase the bubble lifetimes due to the effects of viscosity and surface tension (Kirkpatrick & Lockett, 1974; Sanada et al., 2005). Conversely, surfactants such as sodium dodecyl sulfate (SDS) that are found in oil dispersants significantly inhibit bubble coalescence (Kim & Lee, 1987). As

discussed before, direct observations on the bubbles near the surface by a high-speed camera have shown that coalescence is rare under the present conditions for all bubble sizes.

Another factor, presumably most important, that has been shown to suppress the jetting process is the viscous damping of the capillary waves on the surface of the cavity (Lee et al., 2011; Walls et al., 2015). The critical bubble diameter (d_b^c) below which the jetting is suppressed has been expressed as a critical Ohnesorge number, $Oh^c=\mu/(\sigma\rho d_b^c/2)^{0.5}$, which falls in the 0.037-0.052 range. The resulting values of d_b^c at Oh^c=0.052 (Lee et al., 2011) are also listed in Table 1 for the different liquids involved in the present study. As is evident, d_b^c=10.3 μm for seawater, but increases to 2 mm for crude oil. Hence, for the baseline seawater cases, such damping is less likely to affect the present bubble plumes. As the bubbles rise through the various oil layers, they are expected to pull with them a layer of water, as numerous numerical and experimental studies have shown (Bonhomme et al., 2012; Dietrich et al., 2008; Kemiha et al., 2007). Based on available data on the drainage time of this water layer, it is reasonable to expect that the liquid surrounding the bubble consists of a mixture of contaminant and water, and that the fraction of water decreases with increasing layer thickness. Given the very high d_b^c for crude oil, the 2-3 times reduction in EF_n for the 50 μm oil slick at all sizes, and the striking two orders of magnitude decrease for the 500 μm layers should be expected. Consistent with our visual observations during the experiments involving jet formation, the crude oil layers greatly suppress the jet droplet generation, especially for the 500 μm slick, in clear contrast to the baselines. Considering that the bubbles are more likely to burst in regions with less oil, e.g. after running the plume for a while, it raises questions about the oil content in the droplets and atmosphere above the slicks. This question has prompted the measurements discussed in the Supporting Information that confirm the presence of oil in the airborne particles.

As demonstrated before, the introduction of dispersant, with or without oil, also reduces the number of micron-sized particles, especially below ~2.5 μm (Figure 10). The same size constraint persists for the medium and small bubble plumes, and becomes increasingly sharper during the transition from 50 μm to 500 μm DOR 1:25 layers and to the 50 μm slick of pure dispersant. Several physicochemical processes are likely to be involved. First, due to its high viscosity, d_b^c for pure dispersant is very large (Table 1), suggesting that bubble bursting is not likely to occur if the Corexit 9500A layer is sufficiently thick. Since this dispersant is soluble in water, as the (50 μm) pure slick begins to dissolve it creates a thicker layer with concentration-dependent elevated d_b^c. This observation does not apply to

the DOR 1:25 oils, for which d_b^c is not substantially different from that of pure crude oil, yet their EF_n size distributions are drastically different. Second, as the bubble drags a water layer into the DOR 1:25 oil slick, the liquid-liquid interface is expected to break up rather rapidly (Brandvik et al., 2014; Lessard & DeMarco, 2000; Li et al., 2011; National Research Council, 2005) because of the low interfacial tension. For oil droplets in water, the typical droplet size for high dispersant concentration is in the order of 2 μm (Gopalan & Katz, 2010). However, such a breakup process does not occur in the absence of oil, yet the distinct cutoff at ~2.5 μm persists in both. Third, dispersants not only contain surfactants that reduce the surface tension of the water, they also form a mono-layer known to stabilize the bubble, increase its skin friction, and slow down gas diffusion across its interface (Fdhila & Duineveld, 1996; Jamnongwong et al., 2010; Rosso et al., 2006). Accordingly, prior studies (Boulton-Stone, M, 1995; Dey et al., 1997; Lewis; & Schwartz;, 2004; Veron, 2015) have shown that both EF_n and ejection height decrease in the presence of surfactants, the latter being consistent with qualitative observations during the present measurements (not shown). While these observations agree with the reduction in EF_n with increasing dispersant concentration, they do not explain the preferred size. Can the combined effects of viscous damping and formation of a surfactant monolayer restrict the bursting and jetting to bubbles exceeding a certain size? Answering this question is deferred to future controlled studies.

4.2 Sub-micron particle emissions

This discussion seeks plausible explanations for trends of the sub-micron particle distributions observed in the large and small tank experiments, both in ambient and clean air. In ambient air, the sub-micron particle concentrations increase by an order of magnitude in the large tank only when large bubbles burst in pure dispersant or 500 μm thick oil-dispersant slicks (Figure 3-4). However, in spite of this substantial increase, for each of the replicated tests, which have different initial size distributions of ambient particles, the shape of this size distribution persists during and after bubble injection. Similar trends have been observed in the small tank, i.e., in spite of the increase in the concentration of aerosolized nano-particles, the different shapes of the size distribution persist during and after bubble injection. In pursuit of a plausible explanation, we have examined the surface of 5 mm deep seawater samples placed in transparent flasks with 8mm airspace above them under a microscope at a 40x magnification (0.09 μm/pixel). The air is circulated above the surface at a rate consistent with that of the SMPS sampling rate. Sample images comparing the surfaces at the beginning of the tests and 10 min later are provided in Figure 13. For seawater exposed to ambient air

(Figure 13a &b), there is no accumulation of particles visible on the surface. In contrast, for ambient and seawater premixed with dispersant at a concentration of 0.17 mg/L (Figure 13c &d), which is consistent with that of a 50 μm dispersant layer in the small tank, there is a substantial accumulation of particles on the surface. In fact, the 237x199 μm sample contains well over ~2000 particles, many of them in the submicron range. For seawater premixed with dispersant at the same concentration exposed to clean air (Figure 13e &f), there is no change in the visible concentration of particles on the surface, although both the initial and final images show white spots, which are presumably associated with the early formation of emulsions. These observations suggest that in the presence of dispersant and ambient air, there is a substantial accumulation of particles on the water surface. Such accumulation clearly does not occur for water without dispersant or in clean air. Hence, we postulate that the presence of dispersant affects the accumulation of ambient particles on the water surface. These particles could then become the source for the increased concentration of airborne nano-particles upon exposure to the large bubbles, without changing the shape of their size distribution. We recognize that this claim is speculative at this point, requiring an explanation for the mechanisms involved, and how they are affected by particle and dispersant properties. Such analysis is deferred to future studies.

Reasons for why this phenomenon occurs only for large bubbles may involve a difference in the bursting process, i.e., formation of film droplets versus jet droplets (Veron, 2015). Since only large bubbles (>500 μm) cause the nano-scale increase, presumably, the formation of film droplets plays a role. It has already been shown that the thin caps above rising bubbles have a smaller thickness in the presence of surfactants (Modini et al., 2013). Consequently, the dispersant might also facilitate the resuspension of particles without them being part of larger droplets. In contrast, the small bubbles mostly generate larger jet droplets and contain more of the bulk liquid (Keene et al., 2007; Veron, 2015). Hence, they are less likely to eject nano-particles located on the surface.

The decay rate in concentration after bubble bursting stops is slow in the presence of ambient air in both facilities. However, padding the tank wall with oil absorbers accelerates the decay rate, bringing it to the same level as that of clean air (Figure 7). This trend suggests that the tank walls might also be sites for the particle deposition. Support for this postulate comes from a recent study (Vohra et al., 2017) showing that dry CsI aerosols deposit on the walls of an enclosed acrylic chamber. It is plausible that some of the airborne oil-water-dispersant-particle mixtures suspended by the bubble-bursting deposit on the wall of the tank.

Once bubble injection stops, the tank walls presumably dry, causing resuspension of these particles. Hence, the shape of the size distribution after bursting stops remains the same as that of the original ambient particles. Explanations for the initial short delay in decay would be speculative, e.g. some particles settling on the padding on in interior pipes of the SMPS.

There is also a substantial increase in sub-micron airborne droplet concentration in the presence of clean air for the cases involving dispersant. However, the concentrations involved (Figures 5 and 6) are much smaller than those observed with ambient air (Figure 4), and the associated mass emission is very small. In this case, the size distribution has a persistent single mode at 120-130 nm. This is consistent with the previously observed range of 100-135 nm film droplets generated in clean seawater (Lewis; & Schwartz;, 2004; Mårtensson et al., 2003) as well as the 110 nm film droplet mode reported for clean and SDS-contaminated seawater (Sellegri et al., 2006). While these nano-sized film droplets are presumably generated by the large bubbles also in the presence of ambient air, their concentration is orders of magnitude smaller than that of the sub-micron particles in ambient air.

In terms of relevance to open ocean conditions, this paper shows that in the presence of dispersant, bursting bubbles large enough to generate film droplets enhances the nano-particle concentration above an oil slick. The increase is modest for clean air, but may reach an order of magnitude for air containing ambient nano-particles, which commonly occurs in the oceanic environment (Veron, 2015). Extreme cases may include e.g. periods of *in situ* burning of oil after a spill (Buist, 1994), where the air is filled with soot particles.

Acknowledgments, Samples, and Data

This research was made possible by a grant from the Gulf of Mexico Research Initiative. Data are publicly available through the Gulf of Mexico Research Initiative Information & Data Cooperative (GRIIDC) at https://data.gulfresearchinitiative.org (doi: <10.7266/N 77H1GZG>). The authors wish to thank Brandon Fielder for assistance in conducting the experiment, Dr. Yury Ronzhes for the design of the vertical tank facility and the small-scale bubble chamber. The authors wish to acknowledge Dr. Kevin Wepasnick, Anderson Materials Evaluation Inc. for suggesting the protocol for FTIR-ATR analysis using TSP filter samples and assisting in data analysis and interpretation. The authors also thank Dr. Joel A Tang, NMR-JHU for his guidance during FTIR measurements. The authors acknowledge Reviewer #1 (anonymous) for a rigorous and persistent review of the

manuscript throughout, enabling its substantial overall improvement and Reviewer #2 (anonymous) for valuable suggestions enhancing the interpretation of the present results, including the slow decay rates for the nano-size distributions.

References

Afshar-Mohajer, N., Li, C., Rule, A. M., Katz, J., & Koehler, K. (2018). *A laboratory study of particulate and gaseous emissions from crude oil and crude oil-dispersant contaminated seawater due to breaking waves*. *Atmospheric Environment* (Vol. 179). Pergamon. https://doi.org/10.1016/J.ATMOSENV.2018.02.017

Atherton, T. J., & Kerbyson, D. J. (1999). Size invariant circle detection. *Image and Vision Computing*, *17*(11), 795–803. https://doi.org/http://dx.doi.org/10.1016/S0262-8856(98)00160-7

Balston OEM. (2015). *Balston OEM Disposable Filter Solutions*.

Beyer, J., Trannum, H. C., Bakke, T., Hodson, P. V., & Collier, T. K. (2016). Environmental effects of the Deepwater Horizon oil spill: A review. *Marine Pollution Bulletin*, *110*(1), 28–51. https://doi.org/10.1016/j.marpolbul.2016.06.027

Blanchard, D. C. (1989). The size and height to which jet drops are ejected from bursting bubbles in seawater. *Journal of Geophysical Research*, *94*(C8), 10999. https://doi.org/10.1029/JC094iC08p10999

Blanchard, D. C., & Syzdek, L. D. (1988). Film drop production as a function of bubble size. *Journal of Geophysical Research*, *93*(C4), 3649–3654. https://doi.org/10.1029/JC093iC04p03649

Bonhomme, R., Magnaudet, J., Duval, F., & Piar, B. (2012). Inertial dynamics of air bubbles crossing a horizontal fluid–fluid interface. *Journal of Fluid Mechanics*, *707*, 405–443. https://doi.org/10.1017/jfm.2012.288

Boulton-Stone, M, J. (1995). The effect of surfactant on bursting gas bubbles. *J. Fluid Mech*, *302*(1995), 231–257. https://doi.org/10.1017/S0022112095004083

Bozzano, G., & Dente, M. (2000). Shape and terminal velocity of single bubble motion: a novel approach. *Computer Aided Chemical Engineering*, *8*(C), 649–654. https://doi.org/10.1016/S1570-7946(00)80110-8

Brandvik, P. J., Johansen, O., Farooq, U., Angell, G., & Leirvik, F. (2014). *Subsurface oil releases – Experimental Study of Droplet Distributions and Different Dispersant Injection Techniques - version 2*.

Buist, I. A. (1994). *The science, technology, and effects of controlled burning of oil spills at sea* (Vol. 94). Marine Spill Response Corporation.

C.F.Kientzler, A.H.Woodcock, D.C.Blanchard, & A.B.Arons; (1954). Photographic investigation of the projection of droplets by bubbles brusting at a water surface. *Tellus*, *6*(1), 1–7. https://doi.org/10.3402/tellusa.v6i1.8717

Cachier, H., Buat-Menard, P., Fontugne, M., & Chesselet, R. (1986). Long-range transport of continentally-derived particulate carbon in the marine atmosphere: evidence from stable carbon isotope studies. *Tellus*, *38B*, 161–177. https://doi.org/10.1111/j.1600-0889.1986.tb00184.x

Cini, R., & Loglio, G. (1997). Adsorption and pollutant transport by marine aerosol. *Marine Pollution Bulletin*, *34*(7), 501–504. https://doi.org/10.1016/S0025-326X(97)00031-3

Cipriano, R. J., & Blanchard, D. C. (1981). Bubble and aerosol spectra produced by a laboratory 'breaking wave.' *Journal of Geophysical Research*, *86*(C9), 8085. https://doi.org/10.1029/JC086iC09p08085

D'Andrea, M. A., & Reddy, G. K. (2013). Health consequences among subjects involved in gulf oil spill clean-up activities. *American Journal of Medicine*, *126*(11), 966–974. https://doi.org/10.1016/j.amjmed.2013.05.014

Dey, D., Boulton-Stone, J. M., Emery, A. N., & Blake, J. R. (1997). Experimental comparisons with a numerical model of surfactant effects on the burst of a single bubble. *Chemical Engineering Science*, *52*(16), 2769–2783. https://doi.org/10.1016/S0009-2509(97)00083-3

Dietrich, N., Poncin, S., Pheulpin, S., & Li, H. Z. (2008). Passage of a bubble through a liquid–liquid interface. *AIChE Journal*, *54*(3), 594–600. https://doi.org/10.1002/aic

Ehrenhauser, F. S., Avij, P., Shu, X., Dugas, V., Woodson, I., Liyana-Arachchi, T., et al. (2014). Bubble bursting as an aerosol generation mechanism during an oil spill in the deep-sea environment: laboratory experimental demonstration of the transport pathway. *Environ. Sci.: Processes Impacts*, *16*(1), 65–73. https://doi.org/10.1039/C3EM00390F

Eller, P. M. (1994). *NIOSH manual of analytical methods*. *DIANE Publishing*.

Fdhila, R. B., & Duineveld, P. C. (1996). The effect of surfactant on the rise of a spherical bubble at high Reynolds and Peclet numbers. *Physics of FLuids*, *8*(2), 310–321. https://doi.org/10.1063/1.868787

Flagan, R. C. (1999). On Differential Mobility Analyzer Resolution. *Aerosol Science and Technology*, *30*(6), 556–570. https://doi.org/10.1080/027868299304417

Gill, P. S., Graedel, T. E., & Weschler, C. J. (1983). Organic films on atomspheric aerosol-particles, fog droplets, cloud droplets, raindrops, and snowflakes. *Rev. Geophys.*, *21*(4), 903–920.

Gopalan, B., & Katz, J. (2010). Turbulent shearing of crude oil mixed with dispersants generates long microthreads and microdroplets. *Physical Review Letters*, *104*(5), 1–4. https://doi.org/10.1103/PhysRevLett.104.054501

Guazzelli, E., Morris, J. F., Flanagan, R. C., & Seinfeld, J. H. (1988). Aerosols. *Fundamentals of Air Pollution Engineering*, *45*, 290–357.

Gundlach, E. R. ., & Hayes, M. O. (1978). Vulnerability of Coastal Environments to Oil Spill Impacts. *Marine Technology Society Journal*, *12*(4), 18–27.

de Haar, C., Hassing, I., Bol, M., Bleumink, R., & Pieters, R. (2006). Ultrafine but not fine particulate matter causes airway inflammation and allergic airway sensitization to co-administered antigen in mice. *Clinical and Experimental Allergy*, *36*(11), 1469–1479. https://doi.org/10.1111/j.1365-2222.2006.02586.x

Heyder, J., Gebhart, J., Rudolf, G., Schiller, C. F., & Stahlhofen, W. (1986). Deposition of particles in the human respiratory tract in the size range 0.005-15 μm. *Journal of Aerosol Science*, *17*(5), 811–825. https://doi.org/10.1016/0021-8502(86)90035-2

Hinds, W. C. (1999). *Aerosol Technology, J*. Wiley & Sons New York.

Hu, Y. T., Pine, D. J., & Leal, L. G. (2000). Drop deformation, breakup, and coalescence with compatibilizer. *Physics of Fluids*, *12*(3), 484–489. https://doi.org/10.1063/1.870254

Hyunh, L. X., Briens, C. L., Large, J. F., Catros, A., Bernard, J. R., & Bergougnou, M. A. (1991). Hydrodynamics and Mass Transfer in an Upward Venturi/Bubble Column Combination. *The Canadian Journal of Chemical Engineering*, *69*.

Jamnongwong, M., Loubiere, K., Dietrich, N., & Hébrard, G. (2010). Experimental study of oxygen diffusion coefficients in clean water containing salt, glucose or surfactant:

Consequences on the liquid-side mass transfer coefficients. *Chemical Engineering Journal*, *165*(3), 758–768. https://doi.org/10.1016/j.cej.2010.09.040

Ke, W. R., Kuo, Y. M., Lin, C. W., Huang, S. H., & Chen, C. C. (2017). Characterization of aerosol emissions from single bubble bursting. *Journal of Aerosol Science*, *109*(September 2016), 1–12. https://doi.org/10.1016/j.jaerosci.2017.03.006

Keene, W. C., Maring, H., Maben, J. R., Kieber, D. J., Pszenny, A. A. P., Dahl, E. E., et al. (2007). Chemical and physical characteristics of nascent aerosols produced by bursting bubbles at a model air-sea interface. *Journal of Geophysical Research Atmospheres*, *112*(21), 1–16. https://doi.org/10.1029/2007JD008464

Kemiha, M., Olmos, E., Weiyang, F., Souhila, P., & Z., L. H. (2007). Passage of a Bubble Through a Liquid – Liquid Interface. *Industrial & Engineering Chemistry Research*, *46*, 6099–6104. https://doi.org/10.1002/aic

Kim, W. K., & Lee, K. L. (1987). Coalescence Behavior of Two Bubbles in Stagnant Liquids. *Journal of Chemical Engineering of Japan*, *20*(15), 449.

Kingston, P. F. (2002). Long-term environmental impact of oil spills. *Spill Science and Technology Bulletin*, *7*(1–2), 53–61. https://doi.org/10.1016/S1353-2561(02)00051-8

Kirkpatrick, R. D., & Lockett, M. J. (1974). The influence of approach velocity on bubble coalescence. *Chemical Engineering Science*, *29*(12), 2363–2373. https://doi.org/10.1016/0009-2509(74)80013-8

Kujawinski, E. B., Soule, M. C. K., Valentine, D. L., Boysen, A. K., Longnecker, K., & Redmond, M. C. (2011). Fate of Dispersants Associated with the Deepwater Horizon Oil Spill. *Environ. Sci. Technol*, *45*, 1298–1306. https://doi.org/10.1021/es103838p

Kulkarni, P., Baron, P. A., & Willeke, K. (2011). *Aerosol Measurement: Principles, Techniques, and Applications: Third Edition*. *Aerosol Measurement: Principles, Techniques, and Applications: Third Edition*. https://doi.org/10.1002/9781118001684

Lee, J. S., Weon, B. M., Park, S. J., Je, J. H., Fezzaa, K., & Lee, W.-K. (2011). Size limits the formation of liquid jets during bubble bursting. *Nature Communications*, *2*(May), 367. https://doi.org/10.1038/ncomms1369

Lessard, R. R., & DeMarco, G. (2000). The significance of oil spill dispersants. *Spill Science and Technology Bulletin*, *6*(1), 59–68. https://doi.org/10.1016/S1353-2561(99)00061-4

Lewis;, E. R., & Schwartz;, S. E. (2004). *Sea Salt Aerosol Production: Mechanisms, Methods, Measurements and Models-A Critical Review.*

Lhuissier, H., & Villermaux, E. (2012). Bursting bubble aerosols. *Journal of Fluid Mechanics*, *696*, 5–44. https://doi.org/10.1017/jfm.2011.418

Li, Z., Lee, K., Kepkey, P. E., Mikkelsen, O., & Pottsmith, C. (2011). Monitoring dispersed oil droplet size distribution at teh Gulf of Mexico Deepwater Horizon spill site. *2011 International Oil Spill Conference*, 1–15. https://doi.org/10.7901/2169-3358-2011-1-377

Liyana-Arachchi;, T. P., Zhang, Z., Ehrenhauser, F. S., Avij, P., Valsaraj, K. T., & Hung, F. R. (2014). Bubble bursting as an aerosol generation mechanism during an oil spill in the deep-sea environment: molecular dynamics simulations of oil alkanes and dispersants in atmospheric air/salt water interfaces. *Environ. Sci.: Processes Impacts*, *16*(1), 53–64. https://doi.org/10.1039/C3EM00390F

Major, D., Zhang, Q., Wang, G., & Wang, H. (2012). Oil-dispersant mixtures: understanding chemical composition and its relation to human toxicity. *Toxicol. Environ. Chem.*, *94*(9), 1832–1845. https://doi.org/10.1080/02772248.2012.730202

Mårtensson, E. M., Nilsson, E. D., de Leeuw, G., Cohen, L. H., & Hansson, H.-C. (2003). Laboratory simulations and parameterization of the primary marine aerosol production. *Journal of Geophysical Research: Atmospheres*, *108*(D9), n/a-n/a. https://doi.org/10.1029/2002JD002263

Matson, U. (2005). Indoor and outdoor concentrations of ultrafine particles in some Scandinavian rural and urban areas. *Science of the Total Environment*, *343*(1–3), 169–176. https://doi.org/10.1016/j.scitotenv.2004.10.002

Middlebrook, A. M., Murphy, D. M., Ahmadov, R., Atlas, E. L., Bahreini, R., & Blake, D. R. (2011). Air quality implications of the Deepwater Horizon oil spill. *Proceedings of the National Academy of Sciences*, *109*(50), 20280–20285. https://doi.org/10.1073/pnas.1110052108/-/DCSupplemental.www.pnas.org/cgi/doi/10.1073/pnas.1110052108

Modini, R. L., Russell, L. M., Deane, G. B., & Stokes, M. D. (2013). Effect of soluble surfactant on bubble persistence and bubble-produced aerosol particles. *Journal of Geophysical Research Atmospheres*, *118*(3), 1388–1400. https://doi.org/10.1002/jgrd.50186

Murphy, D. W., Li, C., d'Albignac, V., Morra, D., & Katz, J. (2015). Splash behaviour and oily marine aerosol production by raindrops impacting oil slicks. *Journal of Fluid Mechanics*, *780*, 536–577. https://doi.org/10.1017/jfm.2015.431

Nalco Company. (2008). Corexit Ec9500a Safety Data Sheet, *9300*(800), 10.

National Research Council. (2005). *Understanding Oil Spill Dispersants: Efficacy and Effects*. *National Academies Press*.

Neas, L. M. (2000). Fine particulate matter and cardiovascular disease. *Fuel Processing Technology*, *65*, 55–67. https://doi.org/10.1016/S0378-3820(99)00076-4

O'Dowd, C. D., & de Leeuw, G. (2007). Marine aerosol production: a review of the current knowledge. *Philosophical Transactions of the Royal Society A: Mathematical, Physical and Engineering Sciences*, *365*(1856), 1753–1774. https://doi.org/10.1098/rsta.2007.2043

Parmar, R., & Majumder, S. K. (2013). Microbubble generation and microbubble-aided transport process intensification-A state-of-the-art report. *Chemical Engineering and Processing: Process Intensification*, *64*, 79–97. https://doi.org/10.1016/j.cep.2012.12.002

Resch, F. J., Darrozes, J. S., & Afeti, G. M. (1986). Marine Liquid Aerosol Production From Bursting of Air Bubbles. *Journal of Geophysical Research*, *91*(15), 1019–1029. https://doi.org/10.1029/JC091iC01p01019

Roberts, J. R., Reynolds, J. S., Thompson, J. a, Zaccone, E. J., Shimko, M. J., Goldsmith, W. T., et al. (2011). Pulmonary Effects after Acute Inhalation of Oil Dispersant (COREXIT EC9500A) in Rats. *Journal of Toxicology and Environmental Health. Part A*, *74*(21), 1381–1396. https://doi.org/10.1080/15287394.2011.606794

Rosso, D., Huo, D. L., & Stenstrom, M. K. (2006). Effects of interfacial surfactant contamination on bubble gas transfer. *Chemical Engineering Science*, *61*(16), 5500–5514. https://doi.org/10.1016/j.ces.2006.04.018

Rotenberg, Y., Boruvka, L., & Neumann, A. W. (1983). Determination of surface tension and contact angle from the shapes of axisymmetric fluid interfaces. *Journal of Colloid And Interface Science*, *93*(1), 169–183. https://doi.org/10.1016/0021-9797(83)90396-X

Roth, G. I., & Katz, J. (2001). Five techniques for increasing the speed and accuracy of PIV interrogation. *Measurement Science and Technology*, *12*(3), 238–245.

https://doi.org/10.1088/0957-0233/12/3/302

Rundell, K. W., Hoffman, J. R., Caviston, R., Bulbulian, R., & Hollenbach, A. M. (2007). Inhalation of ultrafine and fine particulate matter disrupts systemic vascular function. *Inhalation Toxicology*, *19*(2), 133–40. https://doi.org/10.1080/08958370601051727

Ryerson, T. B., Aikin, K. C., Angevine, W. M., Atlas, E. L., Blake, D. R., Brock, C. A., et al. (2011). Atmospheric emissions from the deepwater Horizon spill constrain air-water partitioning, hydrocarbon fate, and leak rate. *Geophysical Research Letters*, *38*(7), 6–11. https://doi.org/10.1029/2011GL046726

Sadatomi, M., Kawahara, A., Matsuura, H., & Shikatani, S. (2012). Micro-bubble generation rate and bubble dissolution rate into water by a simple multi-fluid mixer with orifice and porous tube. *Experimental Thermal and Fluid Science*, *41*, 23–30. https://doi.org/10.1016/j.expthermflusci.2012.03.002

Salimi, F., Mazaheri, M., Clifford, S., Crilley, L. R., Laiman, R., & Morawska, L. (2013). Spatial variation of particle number concentration in school microscale environments and its impact on exposure assessment. *Environmental Science and Technology*, *47*(10), 5251–5258. https://doi.org/10.1021/es400041r

Sanada, T., Watanabe, M., & Fukano, T. (2005). Effects of viscosity on coalescence of a bubble upon impact with a free surface. *Chemical Engineering Science*, *60*(19), 5372–5384. https://doi.org/10.1016/j.ces.2005.04.077

Sellegri, K., O'Dowd, C. D., Yoon, Y. J., Jennings, S. G., & de Leeuw, G. (2006). Surfactants and submicron sea spray generation. *Journal of Geophysical Research: Atmospheres*, *111*(D22).

Song, B., & Springer, J. (1996). Determination of Interfacial Tension from the Profile of a Pendant Drop Using Computer-Aided Image Processing2. Experimental. *Journal of Colloid and Interface Science*, *184*, 77–91. https://doi.org/10.1016/S0021-9797(96)90598-6

Spiel, D. E. (1994). The number and size of jet drops produced by air bubbles bursting on a fresh water surface. *Journal of Geophysical Research*, *99296*(15), 289–10. https://doi.org/10.1029/94JC00382

Spiel, D. E. (1997a). A hypothesis concerning the peak in film drop production as a function of bubble size. *Journal of Geophysical Research: Oceans*, *102*(C1), 1153–1161.

https://doi.org/10.1029/96JC03069

Spiel, D. E. (1997b). More on the births of jet drops from bubbles bursting on seawater surfaces. *Journal of Geophysical Research*, *102*, 5815–5821.

Spiel, D. E. (1998). On the births of film drops from bubbles bursting on seawater surfaces. *Journal of Geophysical Research: Oceans*, *103*(C11), 24907–24918. https://doi.org/10.1029/98JC02233

Steffy, D. A., Nichols, A. C., & Kiplagat, G. (2011). Investigating the effectiveness of the surfactant dioctyl sodium sulfosuccinate to disperse oil in a changing marine environment. *Ocean Science Journal*, *46*(4), 299–305. https://doi.org/10.1007/s12601-011-0023-x

Teal, J. (1984). Oil spill studies: A review of ecological effects. *Environmental Management*, *8*(1), 27–43.

Vácha, R., Jungwirth, P., Chen, J., & Valsaraj, K. (2006). Adsorption of polycyclic aromatic hydrocarbons at the air-water interface: molecular dynamics simulations and experimental atmospheric observations. *Physical Chemistry Chemical Physics: PCCP*, *8*(38), 4461–4467. https://doi.org/10.1039/b610253k

Veron, F. (2015). Ocean Spray. *Annu. Rev. Fluid Mech*, *47*, 507–38. https://doi.org/10.1146/annurev-fluid-010814-014651

Vohra, K., Ghosh, K., Tripathi, S. N., Thangamani, I., Goyal, P., Dutta, A., & Verma, V. (2017). Submicron particle dynamics for different surfaces under quiescent and turbulent conditions. *Atmospheric Environment*, *152*, 330–344. https://doi.org/10.1016/J.ATMOSENV.2016.12.013

Walls, P. L. L., Henaux, L., & Bird, J. C. (2015). Jet drops from bursting bubbles: How gravity and viscosity couple to inhibit droplet production. *Physical Review E - Statistical, Nonlinear, and Soft Matter Physics*, *92*(2), 4–7. https://doi.org/10.1103/PhysRevE.92.021002

Wang, X., Deane, G. B., Moore, K. A., Ryder, O. S., Stokes, M. D., Beall, C. M., et al. (2017). The role of jet and film drops in controlling the mixing state of submicron sea spray aerosol particles. *Proceedings of the National Academy of Sciences*, *114*(27), 6978–6983. https://doi.org/10.1073/pnas.1702420114

Wick, C. D., Chen, B., & Valsaraj, K. T. (2010). Computational Investigation of the

Influence of Surfactants on the Air- Water Interfacial Behavior of Polycylic Aromatic Hydrocarbons. *The Journal of Physical Chemistry C*, (Mc), 14520–14527.

Wu, J. (2002). Jet Drops Produced by Bubbles Bursting at the Surface of Seawater. *Journal of Physical Oceanography*, *32*(Wu 1989), 3286–3290.

Yuen, H., Princen, J., Illingworth, J., & Kittler, J. (1990). Comparative study of Hough Transform methods for circle finding. *Image and Vision Computing*, *8*(1), 71–77. https://doi.org/10.1016/0262-8856(90)90059-E

Zhang, M. M., Katz, J., & Prosperetti, A. (2010). Enhancement of channel wall vibration due to acoustic excitation of an internal bubbly flow. *Journal of Fluids and Structures*, *26*(6), 994–1017.

Zhang, Q., & Zhu, Y. (2012). Characterizing ultrafine particles and other air pollutants at five schools in South Texas. *Indoor Air*, *22*(1), 33–42. https://doi.org/10.1111/j.1600-0668.2011.00738.x

Zhang, Z., Avij, P., Perkins, M. J., Liyana-Arachchi, T. P., Field, J. A., Valsaraj, K. T., & Hung, F. R. (2016). Combined Experimental and Molecular Simulation Investigation of the Individual Effects of Corexit Surfactants on the Aerosolization of Oil Spill Matter. *The Journal of Physical Chemistry A*, *120*(30), 6048–6058. https://doi.org/10.1021/acs.jpca.6b04988

Zhou, T., & Liu, H. (2001). Modeling Research of Exposure to Oil Aerosols During Oil Spills. *International Oil Spill Conference*, 6.

Zieger, P., Väisänen, O., Corbin, J. C., Partridge, D. G., Bastelberger, S., Mousavi-Fard, M., et al. (2017). Revising the hygroscopicity of inorganic sea salt particles. *Nature Communications*, *8*(May), 15883. https://doi.org/10.1038/ncomms15883

	Density (ρ) [kg/m^3]	Dynamic Viscosity (μ) [cP]	Surface Tension (σ) [mN/m]	Interfacial Tension with seawater (γ) [mN/m]	Critical bubble diameter (d_b^c) [μm]
Artificial Seawater	1018.3	1.0	73.0	-	10.3
Crude Oil	876.5	8.2	28.0	18.58	2.0×10^3
DOR 1:25 Oil	877.1	10.5	28.0	0.13	3.3×10^3
Dispersant Corexit 9500A	949	66.4@15°C	39-40	0.09	8.8×10^4

Table 1: Physical properties of present liquids at room temperature (unless specified otherwise). Values of ρ, μ and σ are adapted from (Murphy et al., 2015; Nalco Company, 2008; Steffy et al., 2011). The interfacial tension is measured. The critical bubble diameters for jetting are based on $Oh^c = 0.052$ (Lee et al., 2011).

#	Bubble Plume Size [d_b*]	Contaminant	Slick Thick-ness [μm]	Number of Tests in large tank (n)	Number of tests in small tank (ambient air)	Number of tests in small tank (clean air)	Emission Factor (EF_n) per Bubble (large tank data) Mode d_p [μm]	$\sum EF_n$ [#/bubble] [Micro size]
-	**Large [595 μm]**	Baseline	-	5	-	3	1.0	0.32
1	Large	Crude Oil	50	1	-	-	1.1	3.02
2	Large	Crude Oil	500	3	-	3	1.5	1.43
3	Large	1:25 DOR Oil	50	1	-	-	0.8	0.72
4	Large	1:25 DOR Oil	500	3	2	3	1.5	0.40
5	Large	Dispersant	50	3	-	3	--	<0.08
-	**Medium [178 μm]**	Baseline	-	5	-	-	3.5-4.0	8.02
6	Medium	Crude Oil	50	1	-	-	2.7	3.26
7	Medium	Crude Oil	500	3	-	-	1.4-4.6	<0.08
8	Medium	1:25 DOR Oil	50	1	-	-	6.2	3.73
9	Medium	1:25 DOR Oil	500	1	-	-	4.7	1.67
10	Medium	Dispersant	50	1	-	-	2.6, 4.7	1.27
-	**Small [86 μm]**	Baseline	-	5	-	3	2.3-3.0	1.27
11	Small	Crude Oil	50	1	-	-	3.0	0.39
12	Small	Crude Oil	500	3	-	2	1.7	<0.08

13	Small	1:25 DOR Oil	50	3	-	-	4.7	0.64
14	Small	1:25 DOR Oil	500	1	-	2	3.5	0.32
15	Small	Dispersant	50	3	-	2	2.6, 4.0	0.0842.5

Table 2: The test parameters, number of replicated measurements and characteristics of EF_n.

Study	Mode bubble size [d_b*] μm	Mode droplet size [d_p*] μm	Scaling [d_p*/d_b*]	Number of micron/jet drops per bubble [$\sum EF_n$]
Small Bubbles				
Present	86	2.3-3.0	2.67-3.48 %	1.27
(Wang et al., 2017)	60	1.5	2.50%	1.4
(Lee et al., 2011)	53	NA	NA	0-3
Medium Bubbles				
Present	178	3.5-4.0	1.97-2.25 %	8.02
(Veron, 2015; Wu, 2002)	178	4.9	2.75%	6.48
(Lewis; & Schwartz;, 2004)	178	3.23	1.81%	8.82

Table 3: Comparisons of bubble sizes, droplet sizes, droplet scaling and fluxes measured in the present study with those found in other publications for small and medium bubbles.

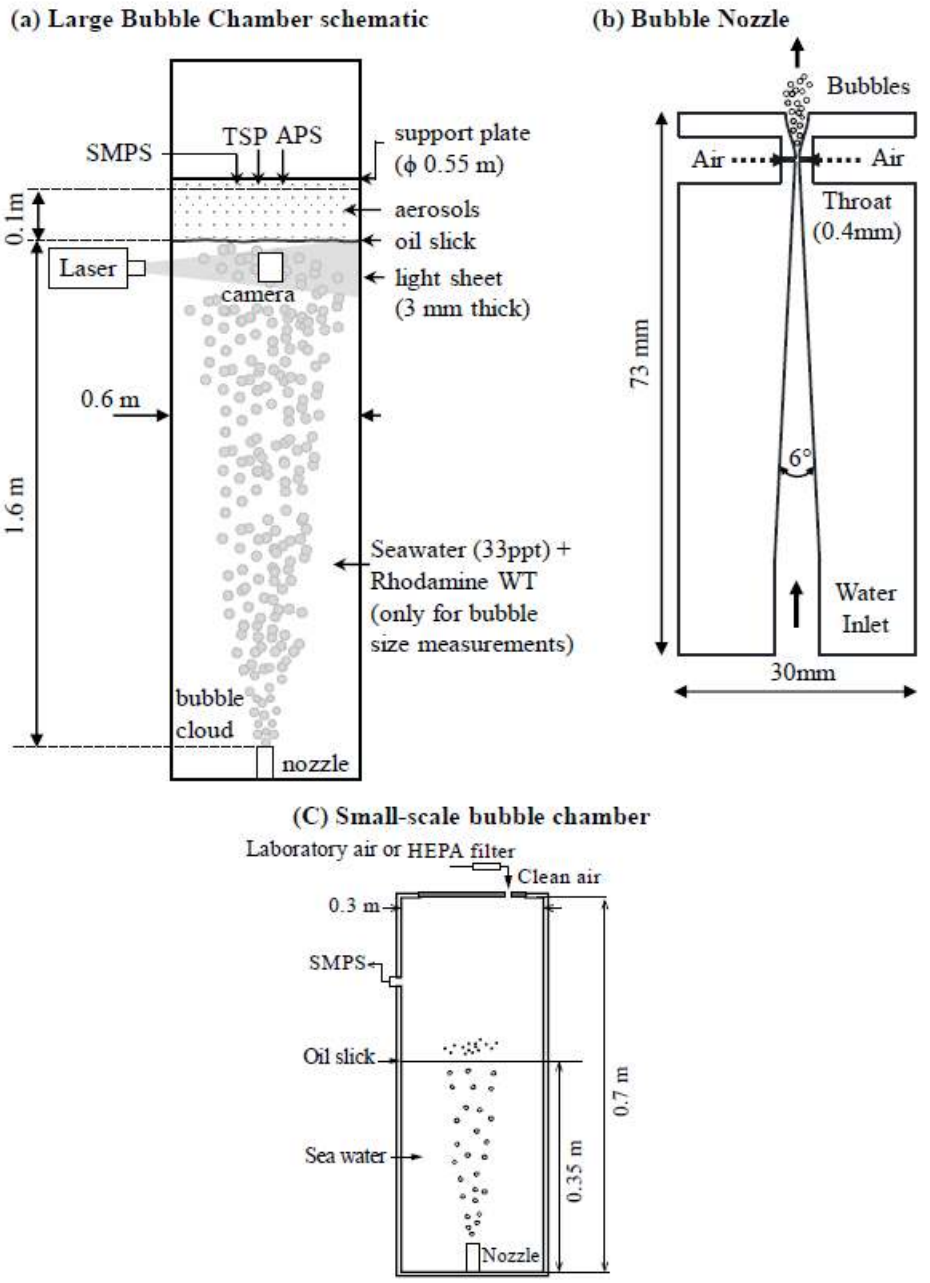

Figure 1: (a) Functional schematic of the large bubble chamber setup used for primary tests. APS: Aerodynamic Particle Sizer, SMPS: Scanning Mobility Particle Sizer, TSP: Total Suspended Particulate mass. (b) Cross-section of bubble generator nozzle. (c) Functional schematic of small-scale bubble-chamber used for auxiliary tests.

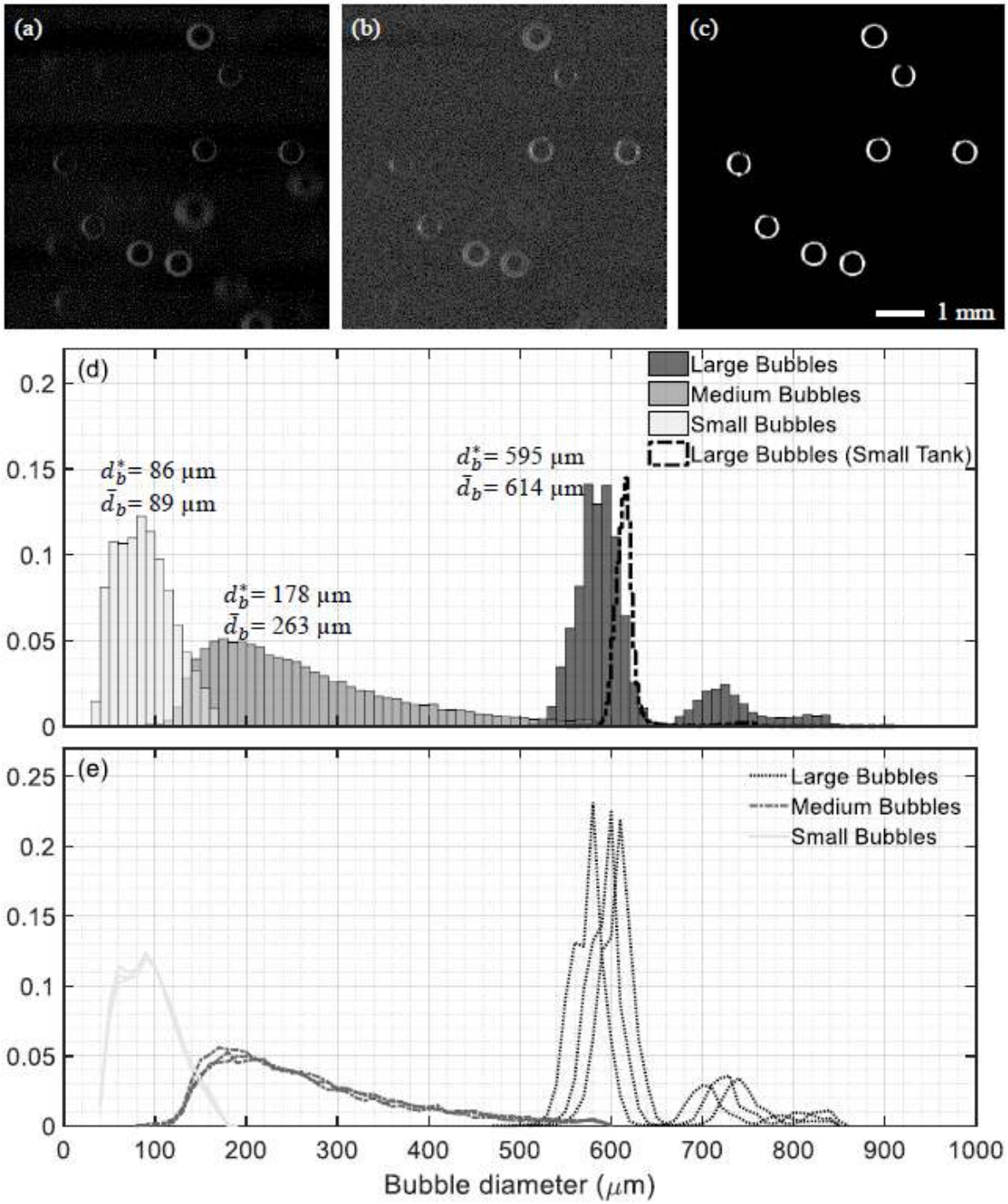

Figure 2: (a) Sample raw image of bubbles in the plume. (b) Intensity gradient of (a). (c) Enhanced image after applying MHE on (a). (d) Bubble size distributions averaged over three independent tests. (e) Bubble size distributions of three replicated tests for each bubble plume. Note: d_b^* and $\bar{d}_b$ denote mode and mean bubble diameters respectively.

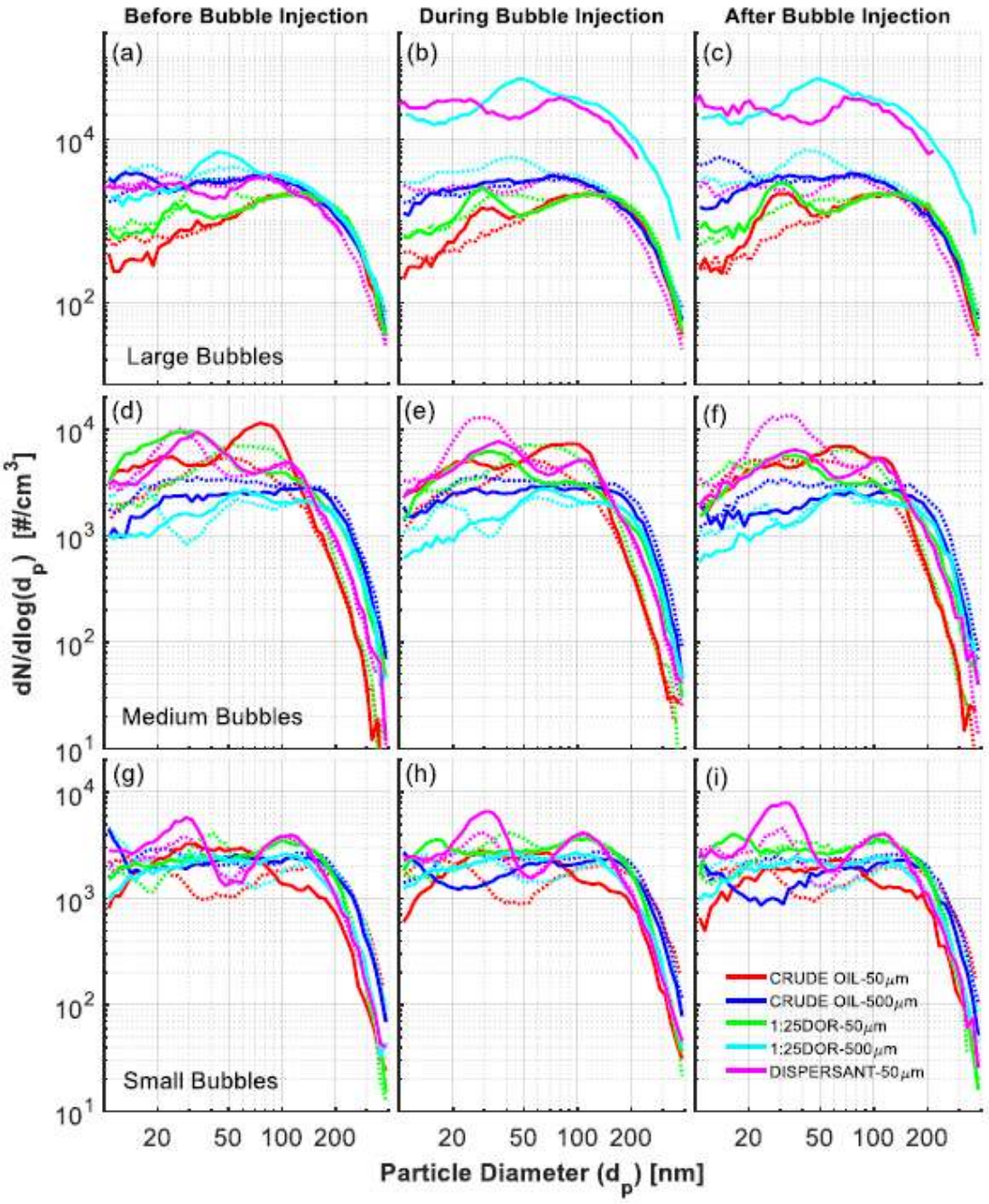

Figure 3: Distributions of nano-sized particle number concentrations [dN/dlog (d_p)] from one out of the available replicated tests for the: (a, b, c) large, (d, e, f) medium and (g, h, i) small bubble plumes in the large tank exposed to laboratory air. Results are time-averaged (a, d, f) 10 min before, (b, e, h) 20 min during and (c, f, i) 10 min after bubble injection. Dotted lines denote baseline runs with a clean seawater surface, and solid lines denote the corresponding tests with oil/dispersant slicks.

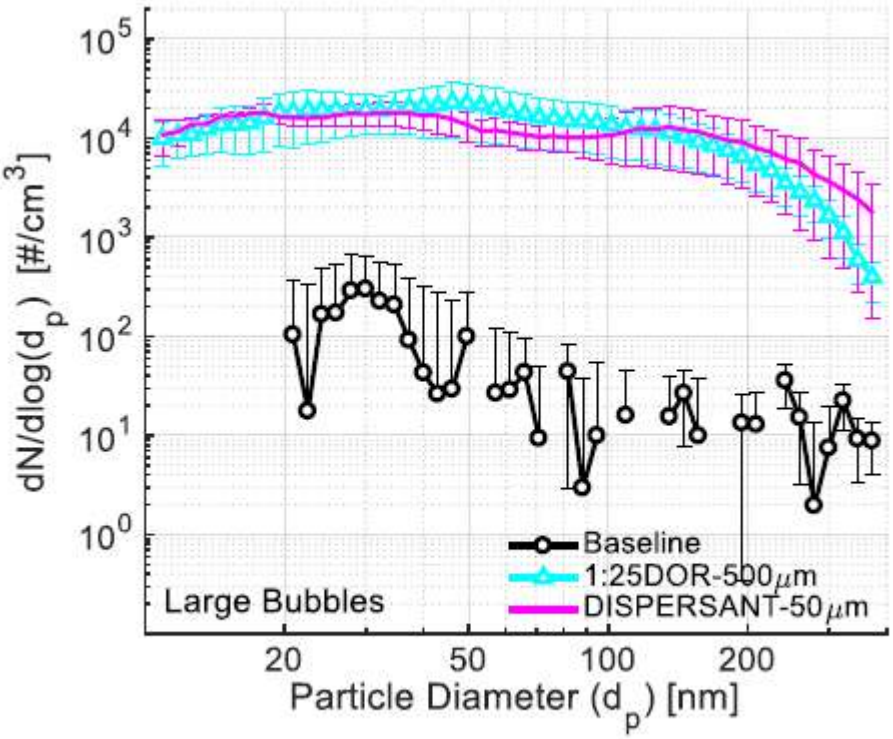

Figure 4: The increase in nano-sized particle number concentrations during bubble injection averaged over time and over three replicated tests performed under the same conditions in the large tank. The background concentrations before bubble injection are subtracted. Error bars denote the standard error among replicates.

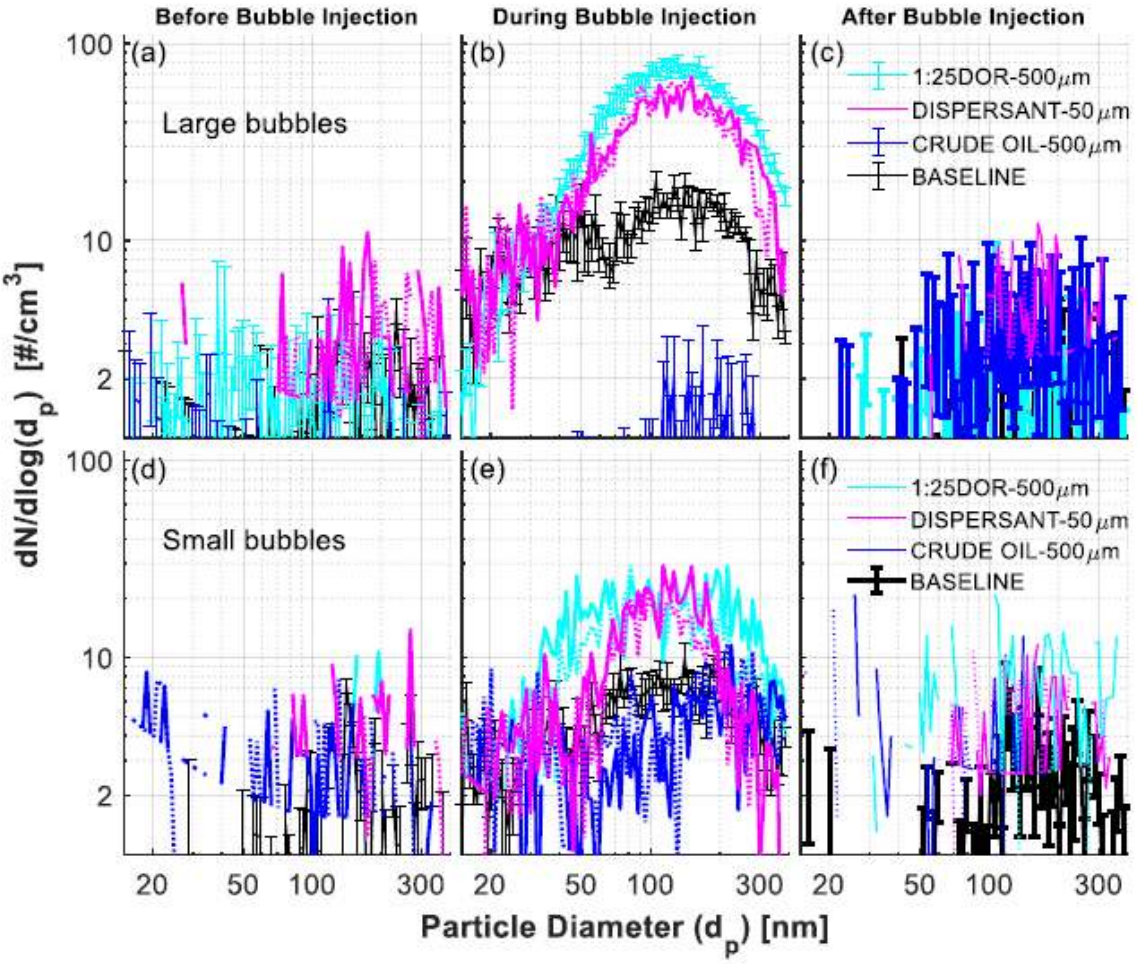

Figure 5: Distributions of nano-sized particle number concentrations for the (a, b, c) large, and (d, e, f) small bubble plumes in the small-scale chamber exposed to HEPA-filtered clean air. Results are time-averaged (a, d) 10 min before, (b, e) 20 min during, and (c, h) 60 min after bubble injection. Cases replicated three times have error bars denoting the standard error among these replicates. Cases with dotted and solid lines of the same color denote two replicated runs. Baseline refers to seawater without a slick.

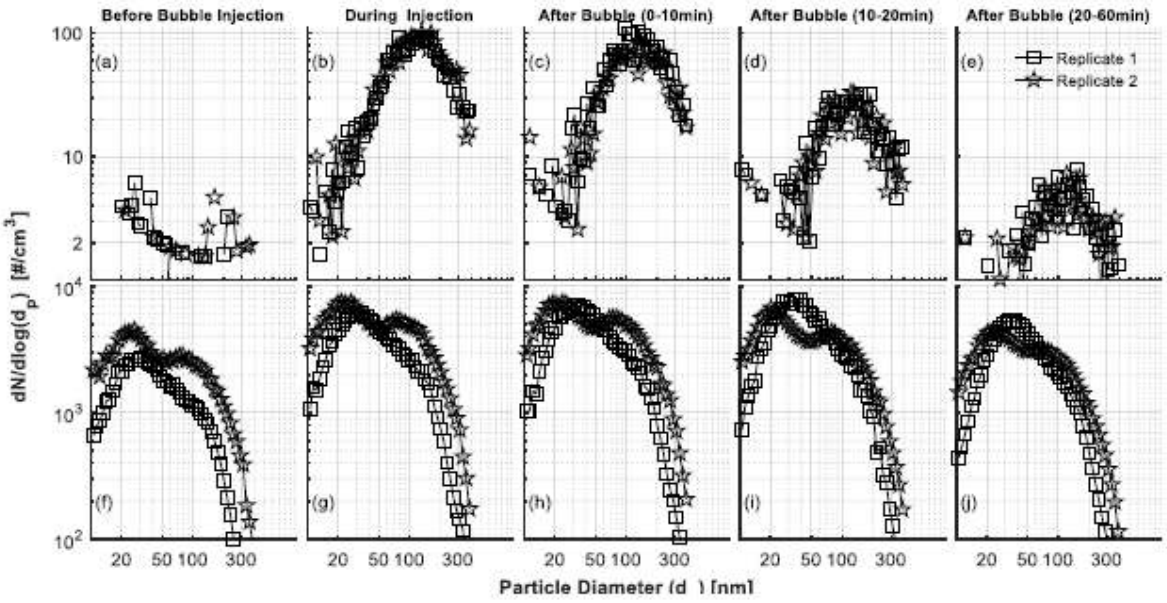

Figure 6: Distributions of nano-sized particle number concentrations for 500 μm thick DOR 1:25 oil slicks with large bubbles in the small-scale chamber. Results from the clean air tests are shown in the first row (a-e), and those corresponding to ambient air tests are shown in the second row (f-j). Each case is replicated twice, and both are shown separately. Results are time-averaged for (a, f) 10 min before bubble injection, (b, g) 20 min during injection, as well as (c, h) 0-10 min, (d, i) 10-20 min and (e, j) 20-60 min after stopping the bubble injection.

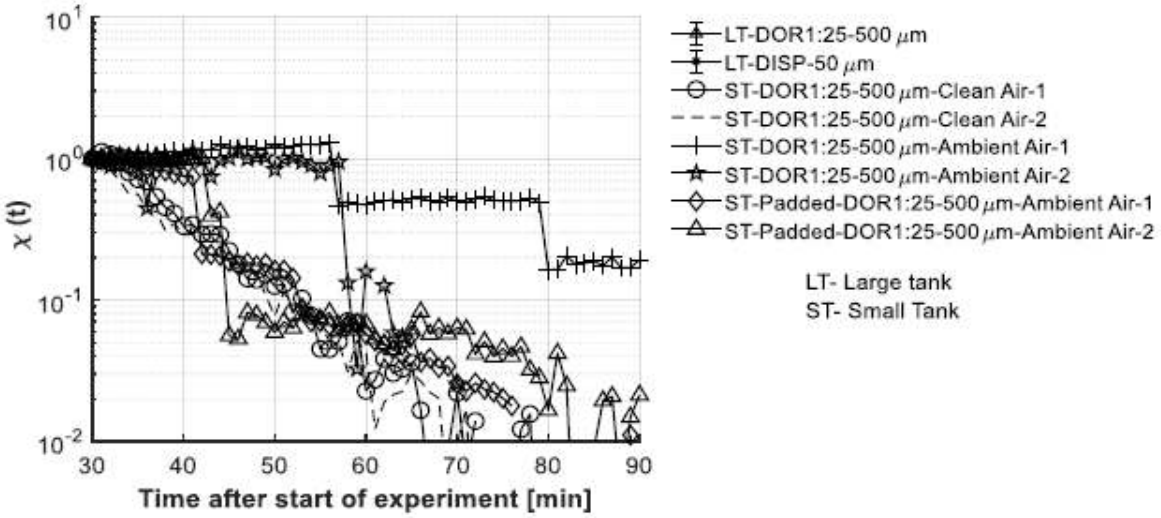

Figure 7: Time evolution of the normalized total nano-aerosol concentration after bubble injection stops, χ(t). The large tank results (LT) are averaged over three replicates, with the error bars denoting the standard error. The small tank (ST) data that have been replicated twice are shown separately. Data for test with padded wall (two replicates) are labeled as ST-padded.

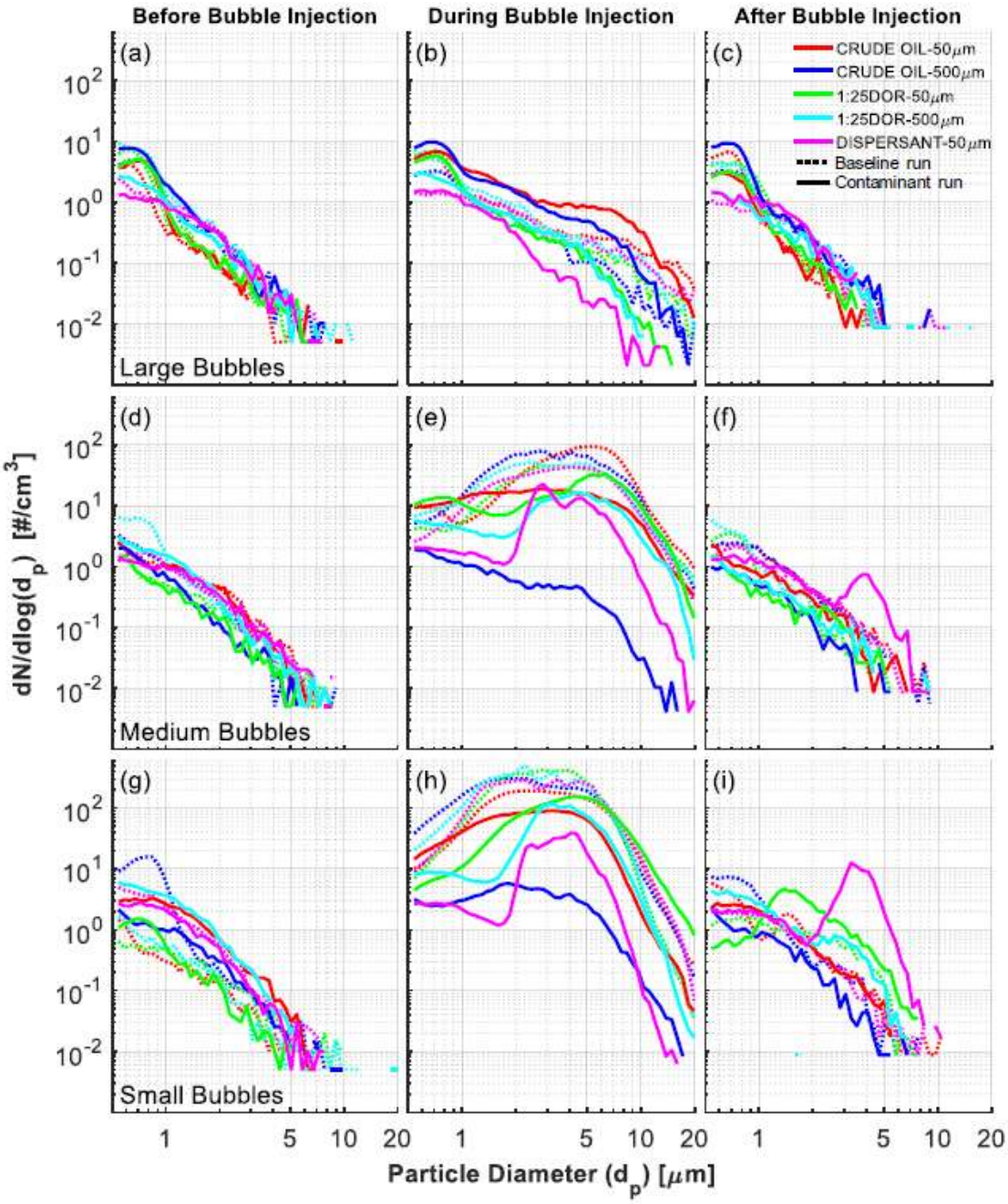

Figure 8: Distributions of micron-sized particle number concentrations [dN/dlog (d_p)] from one out of the available replicated tests for the (a, b, c) large, (d, e, f) medium and (g, h, i) small bubble plumes in the large tank. Results are time-averaged (a, d, f) before, (b, e, h) during and (c, f, i) after bubble injection. Dotted lines denote baseline runs with a clean seawater surface, and solid lines denote the corresponding tests with contaminated slicks.

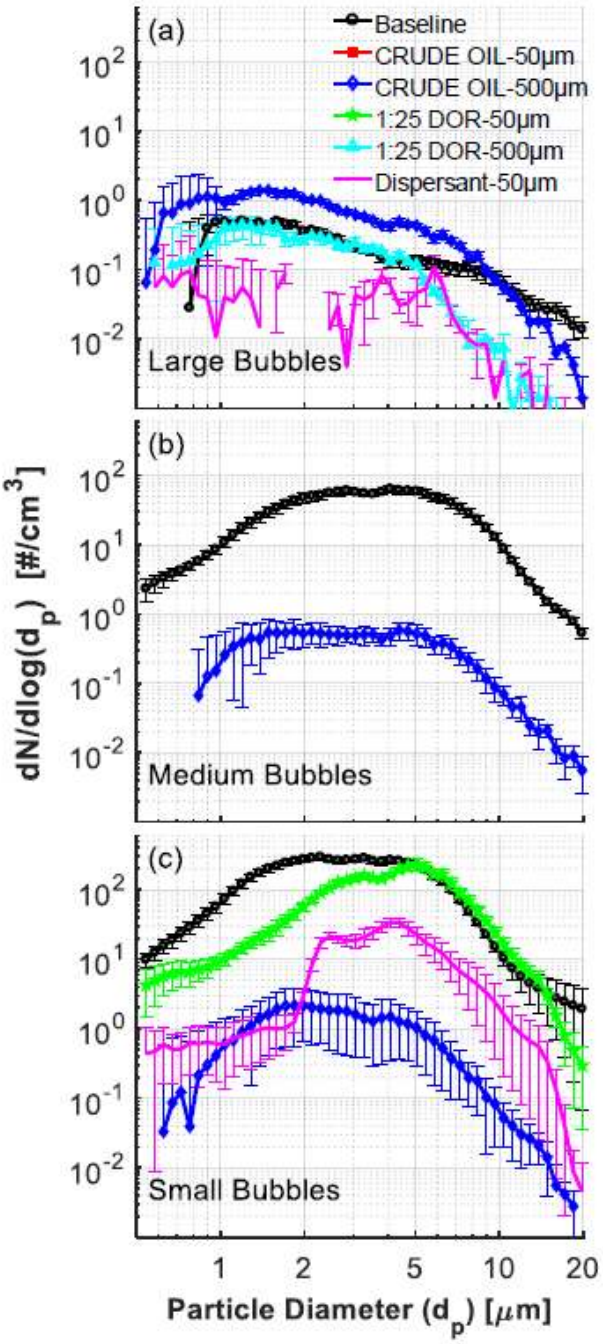

Figure 9: Micron-size particle number concentrations averaged over replicated measurements (Table 2) performed at the same conditions in the large tank. Distributions are time-averaged during bubble injection after subtracting background concentrations before bubble injection. Error bars denote the standard error.

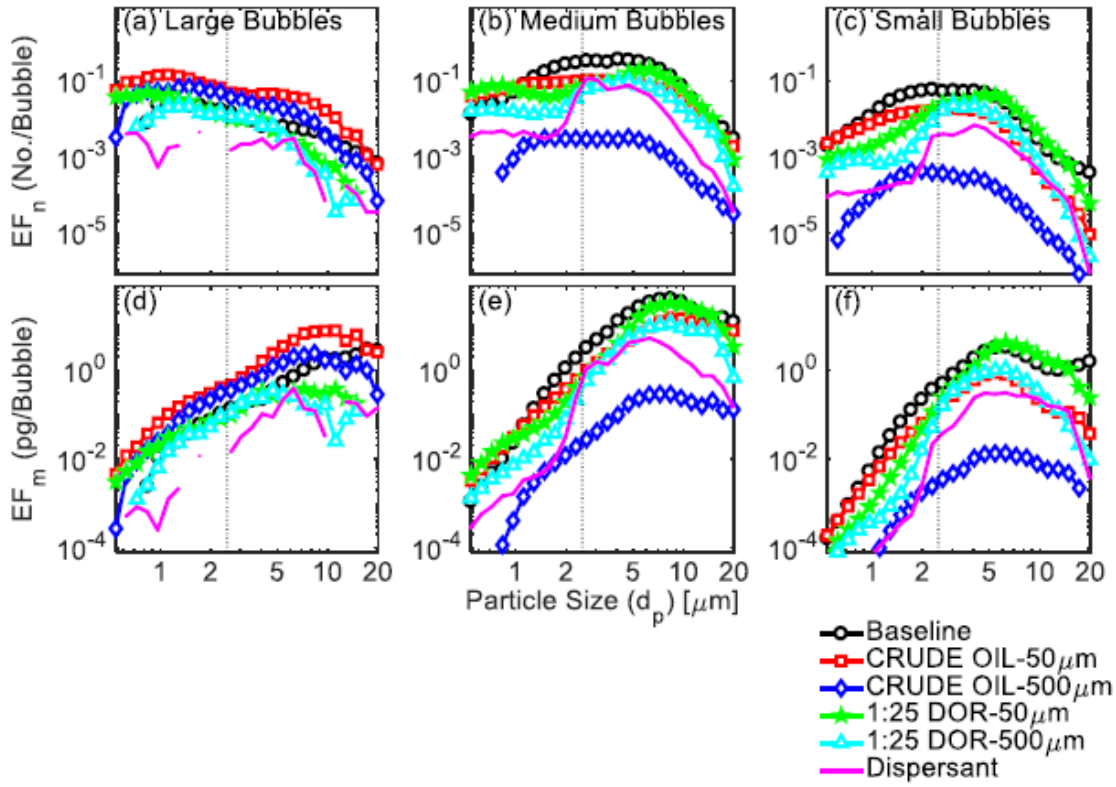

Figure 10: Distributions of EF_n and EF_m in the micron size range for the large ((a) and (d)), medium ((b) and (d)) and small bubble plumes ((c) and (f)) respectively from the large tank data.

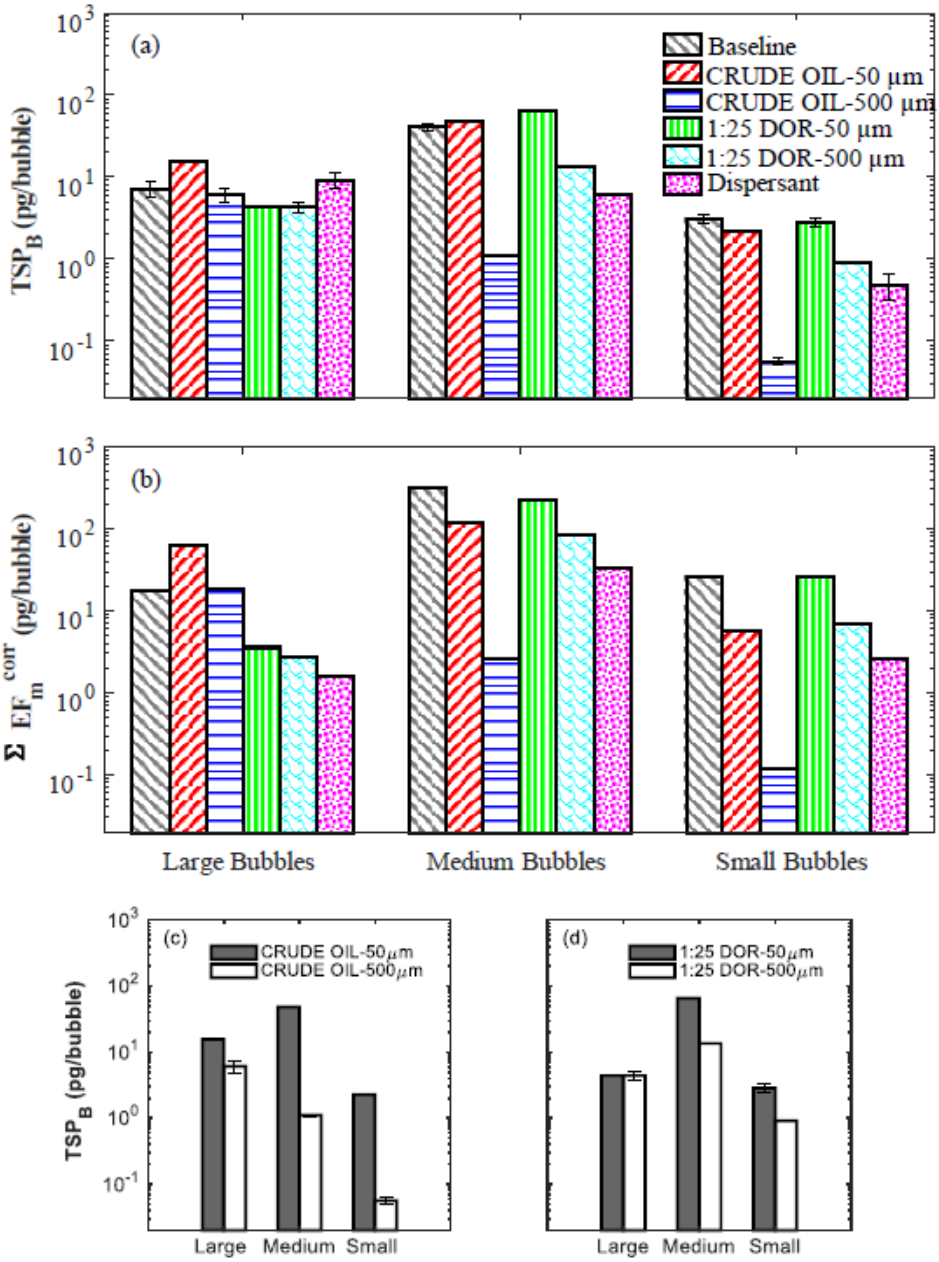

Figure 11: (a) Total suspended particulate (TSP) mass collected per bubble for the large tank tests, denoted as TSP_B. Error bars denote standard error for replicated measurements (Table 2). (b) Distributions of $\sum EF_m^{corr}$ for all the large tank tests with contributions of sub-micron aerosols shown in solid (note log-scale). Distributions of TSP_B from the large tank data for the (c) crude oil and (d) `DOR 1:25 oil slicks, focusing on the effect of slick thickness.

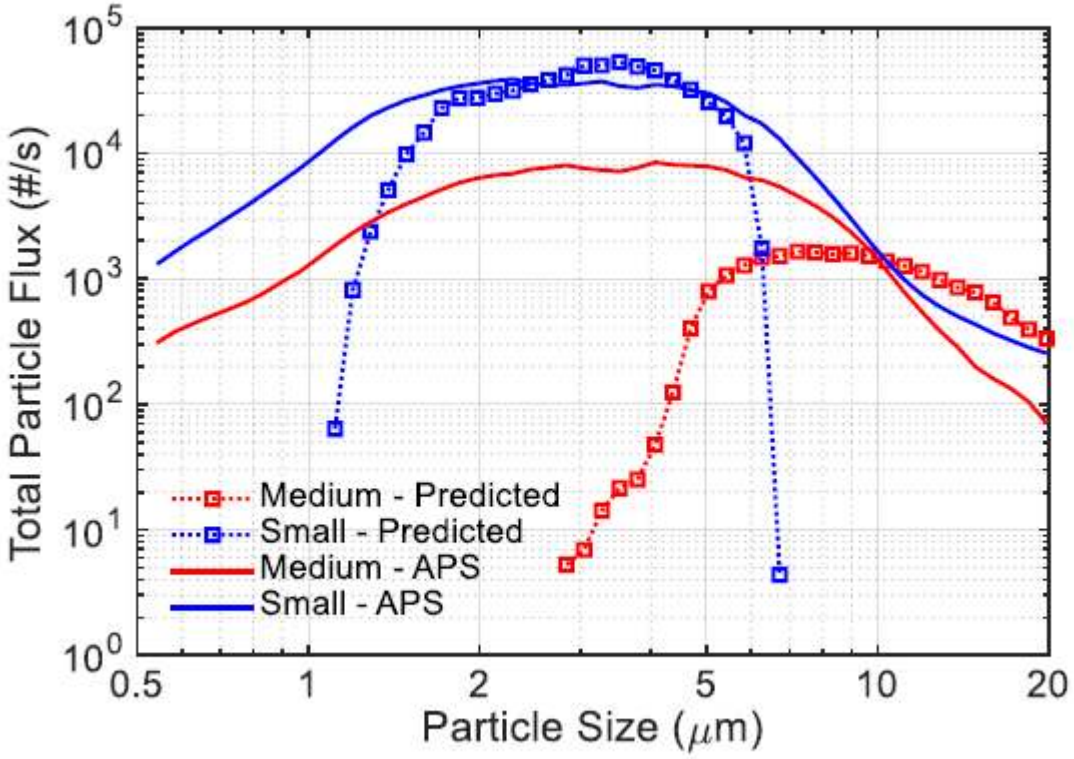

Figure 12: A comparison between the total droplet flux estimated from the APS data (solid lines) for the medium and small bubble plumes to that predicted by the 5% rule (dashed lines), assuming one droplet per bubble.

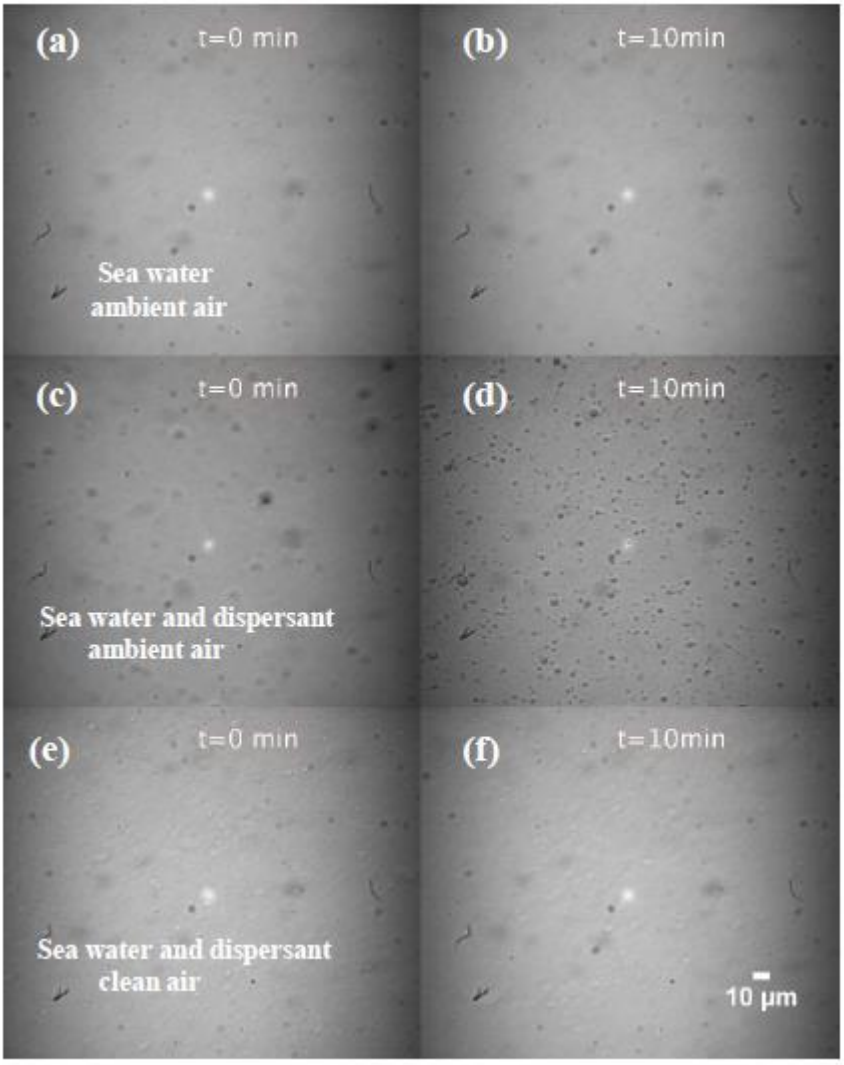

Figure 13: Microscopic (40x) images of air-water interfaces showing the accumulation of ambient particles on the surface (a, c, e) before, and (b, d, f) after exposure to air for 10 min. (a, b) Seawater exposed to ambient air, (c, d) seawater premixed with dispersant (0.17 mg/liter) exposed to ambient air, and (e, f) seawater premixed with dispersant (0.17 mg/liter) exposed to HEPA-filtered air.